

Numerical Simulation of Hardfacing Remanufacturing for Large-Scale Damaged Grinding Roller

liang tian (✉ tl1985212@sjtu.edu.cn)

Tianjin Chengjian University

Shouhang Xing

Tianjin Chengjian University

Guojun Liu

Sichuan Agricultural University

Yu Luo

Shanghai Jiao Tong University

Research Article

Keywords: Hardfacing, Grinding roller, Numerical simulation, Multi-pass welding, Thermal cycle curve, Residual stress

Posted Date: March 5th, 2021

DOI: <https://doi.org/10.21203/rs.3.rs-278299/v1>

License:  This work is licensed under a Creative Commons Attribution 4.0 International License.

[Read Full License](#)

Version of Record: A version of this preprint was published at The International Journal of Advanced Manufacturing Technology on October 2nd, 2021. See the published version at

<https://doi.org/10.1007/s00170-021-08073-4>.

Abstract

The present study is directed to the temperature and residual stresses fields in the hardfacing remanufacturing for a large-scale grinding roller with damage. For this purpose, a numerical procedure for the hardfacing process based on thermal cycle curve method was established, and the effectiveness of the proposed procedure was verified by the measurements of a multi-pass welding experiment with V-groove butt joint. Considering the characteristics of the hardfacing process, a local model of bead-on-plate welding was used to check the heat source and extract the thermal cycle curve. The resulting thermal cycle curve was applied as a thermal load to the corresponding welding layer one by one. Based on the calculated material properties, the data files of the base metal (Grade:KmTBCr26) and the filling layers (Grade:ARCFW9024) were re-developed to define the temperature-dependent physical and mechanical properties of the materials used in the hardfacing remanufacturing. The numerical simulation results reveal the changing trend and distribution of the temperature and residual stress fields during the hardfacing remanufacturing for the damaged grinding roller. The distribution of temperature and residual stress is very complicated due to the numerous welding layers in the hardfacing process. It is pointed out that with the increase of surfacing layers, the heat-affected zone of the grinding roller expands gradually, and the maximum tensile stress always appears at the position near the weld toe, which is prone to fatigue failure or interface peeling due to stress concentration.

1. Introduction

With the rapid development of the power and building materials industry, various types of milling facilities are commonly used to pulverize coal gangues and cement aggregates in large-scale power and cement plants, respectively. The grinding roller are the main working part of the grinding equipment, which has a high damage rate, due to the power-making process is achieved by the squeezing and grinding for the materials placed between them [1, 2], so a regular maintenance and replacement for these working parts becomes a necessity. If the abrasion resistant layers of the grinding roller are largely peeled off or unevenly worn, which will cause the main working parts to almost lose their rolling action. Even worse, the surface cracks in the hardfacing layers spread to the substrate and may even cause the overall fracture of the equipment, resulting in a series of serious production accidents [3, 4]. Therefore, the grinding roller must be repaired or replaced in time after sever wear and tear to guarantee the long-term service safety of the equipment.

The so-called hardfacing technology means that special welding materials with high wear resistance are deposited on the working surface of common metal parts by using built-up welding, so as to improve the mechanical performance of working parts or repair the appearance dimensions of damaged components [5, 6]. For mechanical parts that have exceed the service period or failed, the hardfacing technology can remanufacture them, and significantly improve the resistance of the working surface of remanufactured parts to wear, corrosion and fatigue cracking, and further effectively extend the service life for mechanical products, especially for some special engineering equipments that are in service under severe working conditions [7, 8]. For example, the grinding roller commonly used in large-scale pulverizing equipment are

faced with special working environment and performance requirements. They are usually used as important working parts for crushing raw materials in cement and electric power industries, which have the characteristic of large volume, high economic value and difficult maintenance and replacement. Because the grinding roller directly participates in the process of rolling raw materials, it is very easy to wear and then affect the working performance [9, 10] [11]. In order to ensure the grinding effect, the damaged grinding roller needs to be replaced or repaired, and it is no doubt that it is uneconomical to replace the damaged roller frequently. Therefore, in the actual production, it is more and more common to use the hardfacing technology to remanufacture this kind of wear-resistant parts. Hardfacing remanufacturing usually involves multi-pass welding for wear resistant materials such as high chromium cast iron (HCCI), which is a very complicated thermo-mechanical process due to the large wear-resistant parts to be repaired and the difficult to accurately measure the thermo-physical properties for iron-chromium based alloys [12, 13]. This brings a great obstacle to the numerical simulation of hardfacing remanufacturing for large-scale grinding rollers with damage.

Up to now, many researchers in industry and academia have mainly studied the hardfacing technology from the perspectives of experiment, theoretical analysis and numerical simulation. In the aspect of hardfacing experiment, Deng et al. [14] used plasma transferred arc welding (PTAW) and oxy-acetylene welding (OAW) to deposit a Co-based alloy layer on the surface of heat-resistant steel. The rotating bending fatigue tests were performed at room temperature and 500 °C for PTAW and OAW specimens. It was found that the fatigue strength of OAW specimens at room temperature was lower than that of PTAW ones, which may be due to the higher amount of carbides in OAW coatings. However, the fatigue limits of the two kinds of specimens at 500 °C are higher than those at room temperature due to the increase in ductility with increasing temperature. M.H. Amushahi et al. [15] studied the hardfacing of low carbon steel using a boron-rich cored wire, and arc spraying and gas metal arc welding (GMAW) techniques were used to produce a series of boride-rich coatings on the surface of St52 steel. Microstructure inspection showed that the coatings of arc spraying composed of a uniform laminar morphology, while the coatings produced by GMAW consisted of a mixture of Fe_2B , α -Fe and some FeB, with strong metallurgical bonding to the substrate. S. Chatterjee et al. [16] investigated the welding procedural effect on the cracking sensitivity and performance of interface between the gray cast iron plate (ASTM grade 2500) and the deposited layers. The research results show that the welding procedure and Cr/C ratio of the hardfacing electrode used have a significant effect on the crack length per unit area of the deposits. The use of high nickel electrodes as a buffer layer attributed highest interface bond strength, while low hydrogen type electrodes can also achieve a comparable bond strength at a lower cost. M. Balakrishnan et al. [17] proposed a novel method to enhance the ballistic performance of armour steel welded joints by depositing a soft buttering layer using austenitic stainless steel consumable in between base metal and hardfacing layer. The test results show that the optimized ballistic performance can be achieved when the hardfacing layer thickness is 0.3 times that of the base metal. D. Kesavan et al. [18] used plasma transferred arc (PTA) welding process to deposit the nickel based hardfacing alloy on 316 L stainless steel substrate, and then studied the effects of aging treatment on coating microstructure, wear and corrosion properties. Compared with the as-deposited hardfacing coatings, it was found that the aged

hardfacing coatings are more prone to pitting from the pitting corrosion studies. In addition, there are many experimental studies on hardfacing, mainly focus on different types of hardfacing process (including plasma transferred arc, gas tungsten arc and laser, etc.) [19, 20] [21] [22] [23], hardfacing alloy materials and additives[24] [25] [26] [27] [28] [29] [30], measurement of residual stresses in hardfacing [31] [32] [33], etc.

There are also some researches on the numerical simulation and theoretical analysis for hardfacing process. Sachajdak et al. [34] presented an application of the CFD FVM model for thermal simulation of the GMAW hardfacing process. The developed model achieved realizable compromise between accuracy and calculation efforts for engineering heat transfer analysis, and showed high reliability by thermography measurements particularly for heat transfer around electric arc. Yang et al. [35] investigated the temperature and residual stresses fields of medium-high carbon steel specimen after hardfacing based on a numerical model. The results showed that the compressive stress appears at the surface of the specimen when the martensite transformation occurs at the HAZ and hardfacing layer. Jiang et al. [36] performed a finite element analysis to estimate the residual stress and deformations in the repair weld of a stainless steel clad plate. The research results show that the heat input and welding layer number have great effects on residual stress distribution, and using multi-layer welding and higher heat input can be helpful to decrease the residual stress. At the same time, Jiang et al. [37] also studied the effect of repair weld length on residual stress in the repair weld of a clad plate. It was found that when the repair length increased, the transverse residual stress in the weld and HAZ decreased, but the repair length had little effect on the longitudinal residual stress. In addition, the researches on the numerical simulation for the hardfacing also involve some other aspects, including the formation and evolution of cracks during the solidification of hardfacing layers [38], the flow of liquid metal in the molten pool during the hardfacing process [39], and the residual stress evaluation for different types of hardfacing processes and alloys [40] [41] [42] [43]. It should be pointed out that, compared with the experimental study and numerical simulation, the theoretical analysis can obtain the results faster at a less computation cost, but it is often limited to some simple geometry with a large number of assumptions. There are relatively few studies on the theoretical analysis of hardfacing, most of which are based on the principle of welding heat transfer to determine the temperature distribution of hardfacing for some specific geometric bodies such as cylinder or semi-infinite body, etc. [44] [45] [46], this may be due to the complexity of hardfacing makes it difficult to obtain a general analytical formula.

Through a large number of literature investigations, there are many experimental studies on the special flux-cored wire with wear resistance, metallographic structures and mechanical properties of hardfacing layers, but there are few numerical studies on the hardfacing remanufacturing for large grinding rollers with damage. However, the realization of numerical simulation for this remanufacturing process has important practical application value, which can provide a meaningful reference for quantitative evaluation of residual stresses and targeted improvement for the hardfacing remanufacturing process. Therefore, it is necessary to carry out numerical investigations on hardfacing remanufacturing for the damaged grinding rollers, as as to promote the development and application of this repairing technology for wear-resistant engineering components and structures.

In the present study, a numerical simulation procedure for the hardfacing remanufacturing of damaged grinding roller was proposed based on thermal cycle curve method. An appropriate average thermal cycle curve was obtained by the local model of bead-on-plate welding using a thermo-elastic-plastic finite element analysis. The effectiveness of the proposed numerical procedure was validated by a welding experiment with V-groove butt joint. The local and global mesh models of the damaged grinding roller were established, and then the temperature and residual stresses fields in the hardfacing layers and substrate of the grinding roller were analyzed to show areas prone to fatigue failure or interface peeling. The proposed numerical scheme may serve as a tool for prediction the temperature and residual stresses fields to be used as an evaluation standard for the hardfacing remanufacturing of the worn grinding roller.

2. Hardfacing Remanufacturing Of Grinding Roller

In order to facilitate the establishment of a reasonable numerical model for hardfacing remanufacturing of grinding rollers, it is necessary to introduce the hardfacing technology first. At present, in industrial fields such as power plants and cement plants, the material of rollers used is mostly high-chromium cast iron, which has high hardness and good wear resistance, but also has defects such as poor impact resistance and fracture toughness. The thermal stresses generated during the hardfacing process and the performance mismatch between the base material and filler metal will cause uniformly distributed, non-penetrating grid-like cracks on the surfacing layers, as shown in Fig. 1. These evenly distributed surface cracks contributed to the release of thermal stresses and reduce the risk of surfacing layer stripping to a certain extent. However, due to the insufficient stress release, there are still large residual stresses inside the hardfacing layer. These stresses may be superimposed and accumulated with the working stresses under multi loading conditions, causing the surface cracks to expand in different directions until they extend to the base metal of grinding roller to form layered cracks, which may lead to local cavities or extensive spalling in the surfacing layers. Further deterioration of the situation may even cause the grinding roller to suddenly break when the mill is running, two typical failure modes of the grinding roller are shown in Fig. 2.

The so-called remanufacturing engineering is an engineering activity that repairs and transforms the damaged or retired components which still have a remaining life. On the basis of failure analysis and residual life assessment, the use of advanced surface engineering technology can realize the re-service of the end-of-life parts and components. The important feature of this technology is that the quality and performance of remanufactured products should reach or exceed the new ones. In the remanufacturing process of grinding rollers, the high abrasive flux-cored wire is usually deposited on the surface of the damaged roller by self-shielded open arc overlaying welding to restore its original size and function, so as to realize the re-service of the damaged roller. According to statistics, the cost of the remanufactured grinding roller is only 30% of that of the new one, but the service life after repair has been increased by nearly 2 times.

There are basically two types of hardfacing remanufacturing for grinding rollers in practical industrial production: off-line hardfacing and on-line hardfacing. Off-line hardfacing refers to the method of disassembling the damaged grinding rollers and transporting them to the production base for hardfacing remanufacturing. It is suitable for wear-resistant components with large abrasion loss and high quality requirements for remanufacturing. Figure 3 shows the off-line hardfacing for grinding roller of ZGM113K coal mill. The so-called on-line hardfacing remanufacturing refers to the direct use of surfacing equipment to repair the damaged components on site with flux-cored wire open arc welding without disassembling the grinding rollers from the mill. On-line hardfacing remanufacturing is suitable for situations where the wear of the grinder mill is not large or needs emergency treatment. Figure 4 shows the on-line hardfacing remanufacturing of the grinding rollers in LM vertical mill.

3. Theoretical Background For Hardfacing Simulation

The hardfacing remanufacturing of the grinding roller requires repeated welding thermal cycles, combining with the large sizes of the parts and the special surfacing alloy powers, the resulting wide range of temperature and stress fields are very complicated. The residual stresses existing in the surfacing layers and the substrate will greatly increase the risk of the wear-resistant layers peeling-off (including the peeling between the surfacing layers and the peeling of the wear-resistant layers from the substrate as a whole), it may even cause the overall fracture of the grinding roller. This is a problem that needs to be studied urgently. However, due to the complexities of the hardfacing remanufacturing process, the conventional theoretical analysis and experimental research are greatly restricted. Therefore, the use of finite element numerical simulation to study the temperature and stress fields in the hardfacing process of the grinding roller has become the first choice. The following introduces the theoretical background involving the numerical simulation of hardfacing remanufacturing for the grinding rollers.

3.1 Thermal cycle curve method

The hardfacing remanufacturing for damaged grinding rollers is essentially multi-layer and multi-pass welding. Although the whole welding process can be dynamically simulated by using moving heat source method, for such large-scale engineering structures as grinding rollers, the excessive computational cost limits its practical application. In order to cope with this dilemma, the thermal cycle curve method was proposed. That is, through welding experiments or thermal elastic-plastic finite element calculations, the thermal cycle curve reflecting the welding heating process is obtained, which is applied as a thermal load to the corresponding single-pass weld, and then the multiple weld beads are loaded one by one. In this way, each weld is equivalent to undergoing a welding thermal cycle, which can not only save calculation costs, but also obtain more accurate calculation results. Considering the characteristics of the hardfacing studied in this paper, it is more appropriate to use the thermal cycle curve method to study the remanufacturing process for the damaged grinding roller.

The hardfacing remanufacturing of grinding rollers usually needs to repeatedly build up dozens of layers or even more wear-resistant weld beads, which leads to complex temperature and stress fields. In the

numerical simulation of multi-pass welding using the thermal cycle curve method, some typical welding joints are selected and their corresponding mesh models are established. After the welding heat source is checked, the thermal elastic-plastic finite element analysis is performed to extract the average thermal cycle curve in the welding zone for corresponding joints. Then the obtained thermal cycle curve is applied to the corresponding weld bead successively as an initial load. The specific implementation process for the multi-pass welding based on thermal cycle curve method is shown in Fig. 5. It should be noted that the thermal cycle curve can also be obtained by welding experiment measurements. If some welds adopt different process parameters (such as different filler wires, interlayer preheating temperature, welding current, voltage, etc.), the thermal cycle curves applied to different welds also have corresponding differences. In a word, the thermal cycle curve used should be able to accurately reflect the welding thermal cycle history experienced by the welds, so as to ensure the reliability of the numerical simulation for multi-pass welding. The case of using thermal cycle curve method to simulate the build-up welding process is shown in Fig. 6.

3.2 Multi-pass welding simulation based on SYSWELD

As a professional welding numerical simulation software, SYSWELD was jointly developed by AREVA and ESI, which fully realized the coupling calculations of mechanical, thermal conduction and metallurgy [47, 48]. In this study, the MPA multi-pass welding module in SYSWELD was used to realize the numerical simulation of hardfacing remanufacturing for the damaged grinding roller. According to the characteristics of the hardfacing process for grinding roller, a suitable finite element model of local joint which can reflect the welding heating process was established. The relevant parameters of the heat source model were adjusted according to the actual hardfacing conditions to calculate the temperature field of the local welded joint. Then, the average thermal cycle curve of the nodes in the cross-section area of the weld was extracted based on the corrected heat source model. After that, the MPA module was called to load the thermal cycle curve to the corresponding hardfacing layer for calculation, so as to obtain the stress and displacement fields in the hardfacing remanufacturing for the grinding roller.

The implementation of welding simulation needs to provide the thermo-physical and mechanical parameters of materials that vary with temperature during the welding process. The material database of SYSWELD provides the thermo-physical and mechanical properties of commonly used steel, aluminum alloy and cast iron, and considers the influence of various metallographic microstructures on the material properties, including ferrite, pearlite, martensite, bainite and austenite, etc., which are represented by different numbers in the database files. The Chewing gum method proposed by ESI is used to define the materials which have not deposited in the welds. This method avoids the element self-locking phenomenon which is easy to occur in the method of killing or activating elements. By giving a minimum value to the relevant parameters such as the elastic modulus, thermal conductivity and specific heat of the weld materials, the undeposited metal material is approximately treated as hot air, which does not affect the deposited welding layers. With the continuous deposition of the welds, the mechanical properties of the undeposited phase return to normal. Some codes definition the thermo-physical properties for not-yet-deposited materials are given below.

Not Yet Deposited Material

TABLES:

FIN TABLES

MATERIAUX:

METALLURGY

PHASE 2

KX(1) = Table 1

KX(2) = Table 2

C(1) = Table 7

C(2) = Table 8

RHO(1) = TABLE 13

RHO(2) = TABLE 14

REACTION

TABLE

1 / 1 20 1.0-12 1500 1.0*-12*

2 / 1 20 1.0-12 1500 1.0*-12*

7 / 1 20 1 1500 1

8 / 1 20 1 1500 1

13 / 1 20 7.82-06 1500 7.29*-06*

14 / 1 20 7.82-06 1500 7.29*-06*

For the hardfacing remanufacturing of the grinding roller studied in this study, the material properties of the grinding roller and the iron-based surfacing alloy are quite special, but these materials are not recorded in the SYSWELD database, so secondary development is needed. To this end, ESI has a special tool named Material-Data-Manager to establish a material database, which can input material properties data in the form of excel tables, and can also modify the plastic strain hardening law of materials. When setting the material properties in the finite element numerical analysis, the material database file with the

format of *.mat can be directly loaded. In this study, the above-mentioned development tool was used to establish the specialized material database required for hardfacing remanufacturing of grinding roller.

3.3 Selection and verification of heat source model in SYSWELD

Choosing a suitable heat source model has an important influence on the effective implementation for welding numerical simulation. As mentioned in Sect. 2, the hardfacing remanufacturing of the grinding rollers studied in this paper adopts self-shielded open arc surfacing process, in which flux-cored wire is used as an electrode, which is equivalent to MIG welding, so a double ellipsoid heat source model is more appropriate. The double ellipsoid heat source model was first proposed by J. Goldak in 1984 [49, 50], which divided the heat source into two ellipsoids along the welding direction, as shown in Fig. 7. This model takes into account the difference in arc heat along the thickness of the plate, as well as the digging and stirring effects of welding beam. Its mathematical formula is as follows:

The heat flux distribution inside the ellipsoid in the front half is

$$q_f(x, y, z, t) = \frac{6\sqrt{3}f_f\eta UI}{ab_1c\pi\sqrt{\pi}} e^{-\frac{3x^2}{a^2}} e^{-\frac{3y^2}{b_1^2}} e^{-\frac{3z^2}{c^2}} \quad (1)$$

and the heat flux distribution inside the ellipsoid in the rear half is

$$q_r(x, y, z, t) = \frac{6\sqrt{3}f_r\eta UI}{ab_2c\pi\sqrt{\pi}} e^{-\frac{3x^2}{a^2}} e^{-\frac{3y^2}{b_2^2}} e^{-\frac{3z^2}{c^2}} \quad (2)$$

Where, η is arc efficiency; I is welding current; U is arc voltage; f_f and f_r are the distribution coefficients of the total input power in the front and rear parts of the molten pool, $f_f + f_r = 2$; a , b_1 , b_2 and c are the distribution parameters of the double ellipsoid heat source model. Among them, a represents the weld pool length, b and c affect the melting width and penetration respectively.

SYSWELD has a built-in double ellipsoid heat source model and provides a professional heat source calibration module - Heat Input Fitting. By checking the heat source parameters, the heat source model used in the welding simulation can be more in line with the actual welding process. For the double ellipsoid heat source model, its parameters are usually determined based on engineering experience and experimental results. The steps of heat source calibration based on SYSWELD are as follows:

1) Firstly, select the initial values of the distribution parameters of the heat source model for trial calculations based on engineering experience. The initial value can be determined by referring to the

proportional coefficient of the experimental measurements of the molten pool when the welding reaches the quasi-steady state;

2) Secondly, compare the temperature field and molten pool obtained in trial calculations with the experimental results, and adjust the parameters of the heat source model in a targeted way;

3) Finally, substitute the correction values of the parameters into the heat source model to calculate the quasi-steady temperature field again, and repeat the adjustments until the appropriate parameters of the heat source model are determined. Save the calibrated heat source model function as a *.fct file for subsequent implementation in the numerical simulation for hardfacing remanufacturing of grinding roller.

4. Verification Of Numerical Simulation Method For Hardfacing

In Sect. 3.1 and 3.2, the thermal cycle curve method and SYSWELD-based multi-pass welding simulation steps are introduced. In order to verify the effectiveness of the above methods applied to hardfacing process, the multi-pass welding of V-groove butt joint in the literature [51] was taken as an example, the thermal cycle curve method was used to implement the numerical simulation of this case, and the numerical results were compared with the experimental measurements.

4.1 Material and welding specimen

It is necessary to introduce the butt welding process with V-groove in the literature [51] in this section, because of an attempt to apply the thermal cycle curve method to the numerical simulation for the multi-pass welding. Chang et al. [51] carried out welding experiment on butt-welded joints with V-groove and used the X-ray diffraction to measure the residual stresses near the welding line. The length, width and thickness of the experimental specimen are 110 mm, 30 mm and 4.5 mm respectively, with a V-shaped groove filled with three layers of welds. The geometry and dimensions of the welding specimen are illustrated in Fig. 8. Seven measuring points, located in the area near the weld, as shown in Fig. 8 and Table 1, were measured by X-ray diffractometer. TIG welding is used to implement the deposition of the three-layer welding in the V-groove joint. This is a simple multi-pass welding case, which is suitable for the verification of the numerical methods used in the research. Table 2 shows the welding sequence and its corresponding process parameters.

The material used in this specimen is carbon structural steel named A36, and its chemical composition is shown in Table 3. A36 is an American standard carbon structural steel with a microstructure mainly composed of ferrite and pearlite, in accordance with the standard ASTM A36/A36M-03A [52]. The temperature-dependent thermal physical properties and mechanical properties of ASTM A36 are shown in Figs. 9 and 10, respectively [51]. However, there is no such material as A36 in the SYSWELD material database. Through comparison, it is found that the chemical composition of S355J2G3 steel in SYSWELD database is similar to that of A36, as shown in Table 4. S355J2G3 is a kind of low-alloy high-strength structural steel that implements the European standard EN10025-2 [53]. In view of the

similarities between the two steels, based on the material properties of S355J2G3 and the secondary development method described in Sect. 3.2, the special data file of A36 was produced by using Material-Data-Manager, which was used to define the material properties in the subsequent numerical modeling of multi-pass butt-joint welding.

4.2 Numerical modeling of the cited case

Establishment of numerical model for multi-pass butt-joint welding were carried out using the thermal cycle curve method in this section. The mesh model of welding specimen was established by using Visual Mesh 8.0, which mainly includes two types: (1) local mesh model for heat source checking and extraction of thermal cycle curve; (2) global mesh model for multi-pass welding simulation. These two kinds of mesh models are shown in Figs. 11 and 12, respectively. Because the size of this specimen is relatively small, the local model has only one layer of weld bead compared with the global model. Considering the computation time and calculation accuracy, the meshes near the weld zone are finer, while relatively coarser meshes are used in the region away from the weld. The number of nodes and elements in the local mesh model are 21297 and 25536, respectively, while those in the global mesh model are 25536 and 27886, respectively. When performing mechanical analysis, it is necessary to impose appropriate constraints on the model to prevent its rigid body displacement and rotation, just as shown in Fig. 13.

4.3 Heat source check and thermal cycle curve extraction

Before implementing the numerical calculation for the multi-pass butt-joint welding, the heat source needs to be checked first to obtain a reasonable heat source model describing the welding heat input. By calculating the quasi-steady temperature field, the distribution parameters of the double ellipsoid heat source model were adjusted according to the method described in Sect. 3.3 to make the weld pool or thermal cycle curve match the actual one. Save the calibrated heat source model function and name it in the format of *. fct. The heat source parameters after calibration are shown in Table 5. The quasi-steady temperature field refers to the state in which the temperature reaches a relative equilibrium during the welding process. The weld morphology obtained in this state can best reflect the correct heat source model. The simulated quasi-steady temperature field is shown in Fig. 14, and the comparison between the simulated molten pool and the experimental one is shown in Fig. 15.

After obtaining the calibrated heat source model, the numerical simulation of the initial weld pass in the local mesh model was performed by calling the heat source function file. The nodes in the cross-section of the weld, as shown in Fig. 16, were used to extract the corresponding welding thermal cycle curves in the quasi-steady state, and then average them to obtain the average thermal cycle curve, as shown in Fig. 17. The comparison between the numerically calculated and experimentally measured thermal cycle curves is shown in Fig. 18. It can be found from Fig. 18 that the maximum temperature in the thermal cycle curve obtained by the numerical calculation is slightly higher than that of the experimental curve, but in general the two curves are in a good agreement. Therefore, the calculated thermal cycle curve can be used for subsequent multi-pass butt-joint welding simulation. When implementing this multi-pass

welding simulation, the parameters such as the start and end time of each layer of weld bead are shown in Table 6.

4.4 Comparison of numerical and experimental results

The thermal cycle curve obtained in Sect. 4.3 was sequentially loaded to each layer of weld according to the welding sequence and time. Accordingly, each layer of weld experienced a welding heating process as a whole based on the thermal cycle curve. Taking the third layer of weld as an example, the temperature distribution of the specimen after the deposition is shown in Fig. 19. It can be seen that the temperature in the molten pool is the highest, with a large temperature gradient, and the temperature away from the weld zone gradually decreases. Each weld will rise to 1311 °C within 1.3 s after the beginning of welding, and the temperature change trend is consistent with the calculated average thermal cycle curve. The displacement in the Z direction was used to measure the angular deformation. Each weld will cause angular deformations after welding, which is due to the uneven heat input on the upper and lower surfaces of the specimen during the welding process, resulting in inconsistent shrinkage. The angular distortions of the specimen after the third welding pass are shown in Fig. 20. The maximum Z-direction of the specimen after the welding of the first, second and third layers is 0.564 mm, 0.886 mm and 1.110 mm, respectively, as shown in Fig. 21. It can be seen from the Fig. 21 that the angular deformation increases with the deposition of the welding layer. Although the subsequent weld pass will make the angular deformation larger on the basis of the previous one, its increases rate will slow down. This is consistent with the research results of Yan [54]. The reason for this phenomenon is that the cooled weld bead provides an obstacle to the continuous deformation of the specimen by increasing the stiffness of the welded joint. In short, the cumulative effects of each weld in multi-pass welding make the deformation more serious than that in single-pass welding.

The residual stresses obtained by numerical simulation were compared with the experimental measurements to verify the effectiveness of the numerical method used for the hardfacing remanufacturing of the grinding roller. The welding test in literature [51] measured the residual stresses of 7 measuring points near the weld area, and the distribution of the measuring points is shown in Fig. 8. In order to facilitate comparison, the measuring path in the numerical model is consistent with that in the welding test, as shown in Fig. 22. The comparison of longitudinal and transverse residual stresses obtained by experiment and numerical simulation is shown in Figs. 23 and 24, respectively. It can be seen from the figures that the peak value of longitudinal residual stress appears near the weld, presenting a tensile stress state of nearly 400 MPa, and a compressive stress state far away from the weld zone; while the peak value of the transverse residual stress is smaller, which also appears in the area close to the weld, about 45 MPa. The transverse residual stress far away from the weld zone gradually decreases and transforms from tension to compression, but it is always smaller in magnitude than the longitudinal residual stress. By comparing the residual stress curves obtained by numerical simulation and experimental measurement, it can be clearly seen that the change trends of the two curves are basically similar, and they are in a good agreement. Only a few measuring points have great differences, which may be caused by a lot of simplifications in the numerical model and experimental measurement errors.

Through comparative analysis, it can be concluded that the thermal cycle curve method used in this study achieves a better balance between the calculation efficiency and accuracy, so it is more suitable for the numerical simulation of the hardfacing remanufacturing of grinding roller.

5. Numerical Modeling For Remanufacturing Of Grinding Roller

Hardfacing remanufacturing of grinding rollers is to repair worn-out but still worthy grinding rollers to make them capable of service again, which is traditionally called surfacing repair. This section takes the HRM2800 grinding roller as an example to conduct numerical simulation, focusing on the temperature distribution and residual stresses field in the grinding roller substrate and hardfacing layers.

5.1 Synopsis of remanufacturing process for HRM2800 grinding roller

Figure 25 shows the HRM 2800 grinding roller with the groove-like wear in the middle of the working surface, made of high-chromium cast iron. The repair process of the worn roller is as follows: First, perform dyeing flaw detection on the base material of the damaged roller to confirm whether there are cracks penetrating through the base material; then use carbon arc gouging to remove the remaining surfacing layers, and use flux-cored wire with high chromium cast iron type to fill the defects such as pits in the grinding roller matrix; finally, an angle grinder is used to smooth the filled buttering layer, and the remaining cavities are filled to the original size layer by layer to complete the remanufacturing of the worn grinding roller. The specific process is shown in Fig. 26. The grinding roller under surfacing repair is shown in shown in Fig. 27. The remanufacturing parameters used for HRM 2800 grinding roller are shown in Table 7. It is worth pointing out that due to the relatively thin buttering, tempering and capping layers, the numerical modeling in this paper focuses on the filling layer which accounts for the majority of the surfacing layers.

5.2 Calculation of material parameters and established of material database

High chromium cast iron is a kind of anti-wear material with excellent performance, which generally refers to the alloy white cast iron with Cr content between 11% – 30% and C content between 2.0% – 3.6%. Compared with alloy steel, it has much higher wear resistance and better toughness and strength than ordinary white cast iron [55].

Up to now, the wear-resistant of high chromium cast iron has been studied mainly by means of experiments. There are few numerical simulations on high chromium cast iron materials, and their high-temperature thermo-physical parameters are also rare, which brings difficulties to the numerical modeling. In this paper, JMatPro is used to calculate various high temperature physical properties of high chromium cast iron and other materials. It is a powerful calculation software for phase diagram and high temperature performances of metal materials. There are different calculation modules for different types

of materials. According to the compositions of the material, the performance parameters that change with temperature during the solidification process can be calculated [56, 57]. The grade of high chromium cast iron used for HRM 2800 grinding roller is KmTBCr26, and its chemical composition is shown in Table 8. When the cast iron module of JMatPro is used for calculation, it is necessary to set reasonable parameters to ensure the calculation accuracy. The calculation module for cast iron is shown in Fig. 28. There are mainly two forms of carbon in cast iron: graphite and cementite (Fe_3C). In white cast iron, almost all carbon exists in the form of Fe_3C . Therefore, the matrix type of cast iron after solidification is set to pearlite. Since only a very small part of the base metal is heated to melt and participates in the molten pool reaction, the thermo-physical parameters when it is fully diffused to the equilibrium state are selected in this paper. The temperature-dependent physical parameters of the base metal KmTBCr26 calculated through solidification are shown in Fig. 29. The hardfacing layers of the remanufactured grinding roller adopt the high chromium cast iron flux-cored wire ARCFW9024 developed by Beijing ARC Xinxing Co., Ltd. Its chemical composition is shown in Table 9, and the calculated temperature-dependent material properties of ARCFW9024 are shown in Fig. 30.

Because there is no function to calculate the mechanical properties of white cast iron in the cast iron module of JMatPro, its mechanical parameters can be obtained by consulting the Ref. [38, 58]. The research data in literature [58] shows that the tensile strength of high chromium white cast iron (Cr content, 34%) at room temperature ($25\text{ }^\circ\text{C}$), $700\text{ }^\circ\text{C}$ and $1000\text{ }^\circ\text{C}$ is 415 MPa, 200 MPa and 50 MPa, respectively. Ma et al. [38] conducted a numerical simulation study on the chromium carbide overlays welded on the surfaces of ASTM A36 steel plate. Because brittle materials generally do not have a yield state, 90% of the ultimate tensile strength at room temperature is defined as its yield strength, while yield strength at other temperatures is obtained by linear interpolation. In this paper, a similar approach was adopted to produce the temperature-dependent yield stress curve of high chromium cast iron, as shown in Fig. 31.

According to the material database development method in Sect. 3.2, the data files of the base metal (Grade:KmTBCr26) and the filling layers (Grade:ARCFW9024) were re-developed based on the calculated material properties, and they were named as W_HighCrCastIron.mat and W_ARC9024.mat, respectively. The developed material data files were loaded in the SYSWELD welding wizard to implement numerical simulation. Due to the fact that the buttering layer and capping layer are generally very thin compared with the filling layers, these two layers are ignored for the sake of simplification. Only two kinds of materials, including base metal and filling layers were considered in the numerical modeling for hardfacing remanufacturing of grinding roller.

5.3 Establishment of mesh model for hardfacing remanufacturing

Establishing a suitable mesh model is one of the key conditions for numerical simulation. When implementing the numerical simulation of grinding roller remanufacturing, it is necessary to establish two types of mesh models, the whole and the local. The geometrical dimensions of the worn roller used for

remanufacturing are shown in Fig. 32, which is the basis for establishing the global mesh model. It is worth pointing out that the purpose of hardfacing remanufacturing is not to connect different structural components, but to modify the surface of the workpiece or to restore the insufficient size caused by wear or machining errors. This process is similar to that of bead-on-plate welding, so in this study, the model of bead-on-plate welding was used to check the heat source and extract the heat cycle curve, and the corresponding geometric model is shown in Fig. 33. For the sake of simplification, it is approximately considered that the wear area of the grinding roller and the wear-resistant weld beads are rectangular, which does not affect the understanding for the distribution regularity of temperature and residual stress caused by hardfacing remanufacturing. Since the grinding rollers used in industrial production are generally large and the wear-resistant layers are thick, it needs a large amount of computing resources to carry out the overall 3D finite element analysis, so a 2D plane strain model of grinding roller was used for numerical simulation of hardfacing remanufacturing. The number of nodes and elements in the established plane strain model is 72447 and 72346, respectively, as shown in Fig. 34. The mesh model of bead-on-plate welding is shown in Fig. 35. In mechanical analysis, boundary constraints are imposed on the global and local mesh models to prevent rigid body displacement and rotation.

5.4 Thermal cycle curve for hardfacing remanufacturing

In this study, the local mesh model of bead-on-plate welding was used for heat source verification, and the process parameters adopted were consisted with those of hardfacing remanufacturing for grinding roller. Within 2 s after arcing, the temperature field of the bead-on-plate welding enters a quasi-steady state, as shown in Fig. 36, and the morphology of the molten pool basically no longer changes. It can be seen from Fig. 36 that the maximum temperature in the molten pool obtained numerically is about 2000 °C, which is basically consistent with the maximum temperature of the molten pool measured experimentally in the literature [59]. By adjusting the parameters of the heat source model, the simulated weld pool and heat-affected zone are shown in Fig. 37. It is considered that the molten pool will be formed above 1500 °C, which is consistent with the melting temperature of chromium carbide overlays set in literature [38]. The temperature in the heat-affected zone is the austenitizing temperature, which is about 750 °C [60]. The validated heat source model was obtained and saved as a *.fct format file, which was called to simulate the temperature field of the bead-on-plate welding, and the average thermal cycle curve was obtained by averaging the thermal cycle curves of the nodes in the weld cross-section, as shown in Fig. 38. The average thermal cycle curve was saved as a function file named Repair_weld. trc, which was then used to replace the moving heat source for numerical simulation of hardfacing remanufacturing.

5.5 Simulation process and parameters for hardfacing

When the worn grinding roller is remanufactured by hardfacing, the buttering layer needs to be planed to facilitate subsequent processing. In order to simulate the stress release during the planing of the buttering layer, the welding layer W2 is regarded as a planed layer. The first two layers (W1-W2) were overlaid first, then W2 was set as dummy materials to calculate the equilibrium state after removing W2 layer, and then the surfacing process of W2 to W6 was calculated, at this time W1 was regarded as a

filled metal layer. The simulation process of grinding roller hardfacing remanufacturing is shown in Fig. 39.

The welding parameters should be strictly controlled during the hardfacing remanufacturing for grinding roller. It is generally required that the initial temperature of the grinding roller substrate should not be lower than 40 °C. In this study, the preheating temperature and ambient temperature were set to be 40 °C, and the interpass temperature was controlled below 80 °C. Table 10 shows the relevant parameters set in the numerical simulation of hardfacing remanufacturing for the grinding roller.

According to the given calculation process and parameters, the numerical simulation of hardfacing remanufacturing for the grinding roller was carried out. It mainly includes three parts: (1) Numerical simulation of W1-W2 welding layers; (2) Equilibrium calculation of removing W2 layer; (3) Numerical simulation of W2-W6 welding layers. The numerical results were discussed in the following section.

6. Results And Discussion

6.1 Numerical simulation of W1-W2 welding layers

Figure 40 shows the temperature field of the first welding layer W1 at different welding time. It can be seen from this figure that at the initial time $t = 0.245$ s, the whole welding layer W1 starts to heat up, and the maximum temperature that can be reached is about 209 °C. When $t = 4.22$ s, the welding layer W1 heats up to the maximum temperature and then begins to cool down until $t = 15$ s when it drops to about 80 °C, which means the end of a welding thermal cycle. At this time, the base metal temperature at the bottom area connected with the welding layer W1 is higher, up to 250 °C, so that the temperature in the upper part of the welding layer W1 is low and the temperature in the lower part is high, and the temperature difference between the upper and lower layers causes greater thermal stress, which may lead to the delamination between the welding layer W1 and the substrate of the grinding roller. The temperature change of the second welding layer W2 is similar to that of W1, as shown in Fig. 41. Due to the heating of W2 layer, the existing W2 layer is heated again, but the peak temperature is lower than that of the previous thermal cycle. The maximum temperature appears in W1 layer after the surfacing of W2 layer at $t = 30$ s. As the hardfacing process progresses, the heat-affected zone of the grinding roller substrate also expands and extends radially to the depth of the roller. Since the whole heating process is controlled by a given thermal cycle curve, it is ensured that the interpass temperature meets the welding process requirements.

Figures 42 and 43 show the axial (S11), radial (S22) and hoop (S33) residual stresses caused by surfacing W1 and W2, respectively. It can be concluded that the residual stress area caused by the welding layer W2 is larger than that of the welding layer W1. This is because W2 additionally applies a thermal cycle to the substrate and the welds on the basis of W1 heating. It can be seen from Fig. 42 that the peak values of residual stress in the three directions of S11, S22 and S33 caused by W1 are 599, 481 and 751 MPa, respectively, and the peak values of residual stress in the three directions (S11, S22 and

S33) caused by W2 are 600, 493 and 763 MPa, respectively. The residual stress caused by W2 is slightly larger than that of W1. The welding layers W1 and W2 both have a smaller peak value and distribution area for the radial stress (S22), while the peak value and distribution area for the hoop stress (S33) are relatively large. This distribution is similar to the hoop stress in the multi-pass butt welding of 9Cr-1Mo steel pipe conducted by Deng [61], and the magnitude of residual stress is close to that of longitudinal stress in the multi-pass welding of S355J2 thick plate [62]. Excessive hoop tensile stress (S33) will cause a large number of transverse short cracks on the surface of hardfacing layers. It can be seen from these two figures that the residual tensile stress is basically distributed at the junction of the welding layer and the grinding roller substrate, and the maximum tensile stress appears near the weld toe. Correspondingly, there is a balanced compressive stress zone at the bottom and around the tensile stress zone. The axial compressive stress (S11) is basically distributed at the bottom of the tensile stress zone, while the hoop compressive stress (S33) is distributed around the tensile stress zone. As the number of welding layers increases, the stress state in the previous welding layer also changes. After the surfacing of welding layer W2, the tensile stress in W1 decreases correspondingly, and some areas change from tensile stress state to compressive stress state. This is basically consistent with the distribution of residual stress in repair welds for a stainless steel clad plate studied by W. C. Jiang [36].

The grinding roller substrate and hardfacing layers are all brittle materials of high chromium cast iron, so it is suitable to use the maximum principal stress criterion to judge whether the material fails [38]. Figure 44 shows the principal stress distribution of W1 (Fig. 44-a) and W2 (Fig. 44-b). It can be seen that the maximum principal stresses of welding layers W1 and W2 are 751 MPa and 763 MPa, respectively. The stress distribution in the middle of the welding layer is relatively uniform, while the distribution at both ends of the welding layer is quite different. The inner area of the welding layer is generally in a state of tensile stress, while the bottom of the welding layer is in a state of compressive stress, and the maximum tensile stress occurs at the weld toe area where the welding layer connects with the grinding roller substrate. This is due to the sharp geometric transition of welding toe tends to produce stress concentration, which is a part prone to fatigue failure or interface peeling. Therefore, the parts to be repaired should be polished smoothly during hardfacing remanufacturing to avoid sharp geometric transitions. The distribution of principal stress also indicates that the latter welding layer will affect the stress state in the previous welding layer and its surrounding area.

6.2 Equilibrium calculation of removing W2 layer

The welding layer W2 was set as dummy material to simulate the planning process of the buttering layer. Set the material properties and process parameters in the program, call the calculation files of the previous step to restart the numerical calculation. Figures 45 and 46 show the temperature and maximum principal stress distributions before and after the removal of welding layer W2, respectively. It can be seen from the figure that the highest temperature before and after the removal of welding layer W2 is 290 °C and 220 °C, respectively, and the peak principal stress is 763 MPa and 650 MPa, respectively. This indicates that the temperature decreases to a certain extent after the removal of welding layer W2, but its distribution characteristics do not change significantly. After removing the welding layer W2, the

temperature of welding layer W1 is still the highest, and gradually decreases along the radial direction of the grinding roller. The peak value of principal stress still appears at the weld toe connecting the welding layer and the grinding roller substrate, and the inner part of the welding layer is in the state of tensile stress, and gradually changes to the state of compressive stress in the grinding roller substrate. However, due to the removal of the welding layer W2, the distribution and magnitude of the compressive stress have changed. This indicates that the residual stress in the hardfacing repair zone has been released after removing W2 layer, and a new equilibrium state has been reached again.

6.3 Numerical simulation of W2-W6 welding layers

After the calculation of the equilibrium state for the removal of welding layer W2, the mesh model of the grinding roller was updated. Weld layer W1 was defined as the completed group and named as "WELD_FINISHED". The surface elements of the completed welding layer W1 were added to the cooling surface group "AIR", and then the result files obtained from the previous equilibrium calculation were called to restart the engineering files for numerical simulation of welding layers W2-W6. The temperature and residual stress fields in the hardfacing process of welding layers W2 to W6 are discussed below.

6.3.1 Temperature field analysis of welding layers W2 to W6

The hardfacing simulations of welding layers W2 to W6 were carried out on the basis of the equilibrium state calculations. Figure 47 shows the temperature fields of welding layers W2 - W6. It can be seen that the interpass temperature of welding layers W2 to W5 is maintained at 80 °C due to the use of thermal cycle curve to control the welding heating process. The welding layer W6 was kept at room temperature for 30 s after surfacing. Due to the heat conduction between the filled welding layers and W6 layer, the temperature of welding layer W6 is higher than 80 °C, and its maximum temperature is 262 °C, which is lower than that of other welding layers. Generally speaking, the distribution of the temperature field formed by each welding layer is basically similar, the maximum temperature always appears near the bottom of the welding layers, and gradually decreases along the radial direction of the grinding roller, spreading in an arc shape. The temperature at the toe of each welding layer is higher, which will cause greater thermal stress. As the number of surfacing layers increases, the range of the heat-affected zone is also expanding, and the filled welding layers are repeatedly affected by multiple thermal cycles of the subsequent welding layers.

The measuring line located in the middle of the grinding roller, as shown in Fig. 48, is used to measure the temperature of the welding layers from the outer surface to the inner surface. The temperature curves of different welding layers at the points along the measuring line are shown in Fig. 49. It can be seen from the figure that near the outer surface of the grinding roller, since some welding layers (W2 to W5) have not been overlaid, the temperature measured here is actually the ambient temperature, which is kept constant at 40 °C. The shape and magnitude of the temperature curves for the welding layers W2 to W5 are similar, but there is a certain delay between the curves, which is caused by the unfilled welding layers at the temperature points being measured. It can be seen from each curve that when the temperature rises to

about 80 °C, a gentle step area is formed, and the length of the step is the height of the current welding layer. The curves show that the temperature rises rapidly near the bottom of the welding layer, reaching a maximum value of about 300 °C, and the temperature away from the welding layer gradually decreases. However, with the increase of the number of surfacing layers, the heat affected area of the grinding roller expands, resulting in a gradual flattening trend of the temperature curves for the subsequent welding layers. After the surfacing of welding layer W6, the whole grinding roller was kept in the air for 30 s, so the maximum temperature decreased. The change trend of W6 curve is more gentle than that of other curves, which means that the temperature distribution of the grinding roller tends to be uniform after hardfacing remanufacturing.

6.3.2 Residual stress field analysis of welding layers W2 to W6

The maximum principal stress distribution after hardfacing from W2 to W6 is shown in Fig. 50. It can be seen from the figure that the positions of the maximum tensile principal stress in different welding layers are basically the same, and they all appear at the welding toe where the welding layer connects with the substrate of grinding roller, just as shown in the dashed box in the Fig. 50. The inside and bottom of the welding layer are in tensile and compressive stress states respectively, and the residual stresses at the weld toe of the welding layer change from compression to tension. The tensile stress and compressive stress appear alternately in each surfacing layer. The substrate of grinding roller at the bottom and both sides of the hardfacing layers are in the state of compressive stress and tensile stress respectively, and this distribution trend of residual stress is particularly obvious in the welding layer W6.

Two measuring paths were selected for residual stress measurement, as shown in Fig. 51. Path 1 is located in the middle of the hardfacing repair zone of the grinding roller, while path 2 is located at the interface between the surfacing layers and the grinding roller base materials. Figure 52 shows the residual stresses measured along path 1. It can be seen that in the area without hardfacing, the residual stress is zero. With the progress of hardfacing process, the residual stress curves gradually shift to the left. Figures 52-(a), (c) and (d) show axial stress, hoop stress and maximum principal stress, respectively. The curve shapes and changing trends of these three types of residual stresses are similar, but they are different in magnitude. When the measuring points reach the filled welding layers, a large tensile stress appears rapidly and remains stable inside the weld layer area. When the measuring points leave the filled welding layers, it decreases rapidly to the compressive stress, which indicates that there is a large compressive stress area at the bottom of each welding layer after surfacing. With the increase of the measuring distance, the residual compressive stress gradually rises and tends to zero, which shows that the residual stress in the substrate of the grinding roller far away from the hardfacing repair zone is already very small and can be ignored. The stress curves from the welding layer W3 to W6 show a fluctuation from the tensile stress state to the compressive stress state, which is caused by the change of stress state between the latter and the previous welding layer. With the increase of the welding layer, the number of fluctuations between the tensile and compressive stress states also increases, but the amplitude of the stress tends to decrease. This fluctuation of the stress state is particularly obvious in the

curve of the welding layer W6. This is because the numerical calculation of W6 includes a cooling time of 30 s, which plays a crucial role in releasing the residual stress. Therefore, the maximum stress value and stress amplitude of the curve W6 are smaller than those of other welding layers, and the fluctuations between the tension and compression stress states are more regular. Figure 52-(b) shows the radial stresses of different welding layers. It can be seen that the radial stress inside the hardfacing repair zone is all compressive stress, which decreases with the increases of the measuring distance. When it decreases to a certain extent, there is an increasing trend. The radial stress curve of W6 layer is obviously different from that of other welding layers, which is due to the redistribution of residual stress in cooling stage of hardfacing remanufacturing.

Figure 53 shows the residual stress distribution along the measuring path 2, which is significantly different from that along the measuring path 1 in the middle of the hardfacing repair zone. The curves of axial and radial stresses are similar in shape, as shown in Figs. 53-(a) and (b) respectively. It can be seen that there is a large residual tensile stress near the weld toe, and then the tensile stress decreases gradually. There is a relatively large axial compressive stress, while the radial compressive stress is smaller. With the increase of welding layer, the residual stress fluctuates to a certain extent, but the stress amplitude of the latter welding layer is smaller than that of the previous welding layer. This is because the latter welding layer has a heating effect on the previously completed welding layer, which is equivalent to a heat treatment to promote the residual stress release. The curves of hoop stress and maximum principal stress are basically similar in shape, as shown in Figs. 53-(c) and (d), respectively. It can be seen that the residual stress in the area close to the weld toe rises quickly; in the range of the weld layer, the residual stress rises slowly to the maximum; far away from the welding layer, the stress decreases rapidly until the compressive stress appears, but the compressive stress is smaller than the tensile stress in magnitude. Similarly, the axial stress and the maximum principal stress also fluctuate to a certain extent. The amplitude of stress fluctuation decreases in the completed welding layer, but the fluctuation frequency increases with the increase of the welding layers. After the surfacing of welding layer W6, these two types of stress are mainly in tensile state, and the stress distribution tends to be uniform in the grinding roller.

The influence of the number of welding layer on the peak value of residual stress is shown in Fig. 54. It can be seen that the peak residual stress decreases with the increase of welding layer. Compared with the welding layer W1, the hoop, axial and radial residual stresses of W6 layer are reduced by about 23.7%, 30.1% and 56.9%, respectively. This is due to the fact that the thermal effect of the subsequent welding layer is equivalent to applying a stress relief tempering on the completed surfacing layer, which is consistent with the research conclusions drawn by W. C. Jiang et al. [36].

7. Conclusions

In this paper, a numerical simulation procedure was implemented for the hardfacing remanufacturing of worn grinding roller, and the following research conclusions can be summarized based on the research results:

(1) A numerical procedure for hardfacing remanufacturing of damaged grinding roller based on thermal cycle curve method was proposed, and a welding experiment of V-groove butt joint with three-layer welds was used to verify the effectiveness of the proposed numerical procedure. Through the thermo-elastic-plastic finite element analysis, an appropriate average thermal cycle curve was obtained by the local model of bead-on-plate welding, which was applied as a thermal load to the corresponding welding layers in the hardfacing remanufacturing for grinding roller.

(2) The high temperature physical properties of iron-based wear-resistant materials was calculated using JMatPro software. Based on the calculated material properties, the data files of the base metal (Grade:KmTBCr26) and the surfacing layers (Grade:ARCFW9024) were obtained through the secondary development of the material database, which were used to define the temperature-dependent physical and mechanical properties of the materials used in the hardfacing remanufacturing.

(3) The numerical calculation results show that the distributions of temperature and residual stresses fields are very complicated in the hardfacing process, due to the repeated thermal cycles caused by numerous welding layers. In general, the maximum temperature always appears close to the bottom zone of the welding layers, and gradually decreases along the radial direction away from the welding layers. The temperature in the area near the weld toe of each welding layer is higher, which will cause greater thermal stress. As the surfacing layers increase, the heat-affected area of the grinding roller expands, and the filled welding layers are subjected to repeated thermal cycles of the subsequent welding layers.

(4) The number of surfacing layers has a significant effect on the peak value of residual stress. The peak residual stress decreases with the increase of welding layer. Compared with the welding layer W1, the hoop, axial and radial residual stress of welding layer W6 are reduced by about 23.7%, 30.1% and 56.9%, respectively. This can be explained by the fact that the heating of the subsequent welding layer promotes the residual stress release in the previously filled welding layers.

(5) Under the influence of many surfacing layers, the distribution of residual stress shows a great fluctuation in the grinding roller, and the state of residual stress changes between tension and compression with the different positions of surfacing layers. The inside of the welding layer is generally in a state of tensile stress, while the bottom part of the welding layer is generally in a state of compressive stress. The maximum residual stress always appears in the vicinity of the weld toe connecting the welding layer and the substrate, which is easy to cause fatigue failure or interface peeling for the repaired roller, so special attention should be paid to this part in the hardfacing remanufacturing for the damaged grinding roller.

Declarations

Ethical approval:

This material is the authors' own original work, which has not been previously published elsewhere.

Competing interests:

The authors declare that they have no competing interests.

Authors Contributions:

All authors contributed to the study conception and design. Modeling, data collection, and analysis were performed by Liang Tian, Shouhang Xing, and Guojun Liu. The first draft of the manuscript was written by Liang Tian. Yu Luo provided guidance and suggestions.

Consent to participate:

NA

Consent to publish:

NA

References

1. Jensen LRD, Fundal E, Møller P, Jespersen M (2011) Wear mechanism of abrasion resistant wear parts in raw material vertical roller mills. *Wear* 271(11–12):2707–2719
2. Gao H, Qu LG (2002) 3D design and analysis of the crushing roller of a high-pressure grinding roller. *Journal of Materials Processing Tech* 129(1–3):649–652
3. Pareek P, Sankhla VS, Review on vertical roller mill in cement industry & its performance parameters, *Materials Today: Proceedings In Press* (2021) <https://doi.org/10.1016/j.matpr.2020.10.916>
4. Jensen LRD, Friis H, Fundal E, Møller P, Brockhoff PB, Jespersen M (2010) Influence of quartz particles on wear in vertical roller mills. Part I: Quartz concentration. *Miner Eng* 23(5):390–398
5. Parmar RS (2003) *Welding processes and technology*, second edn. Khanna Publishers, New Delhi
6. Balaguru S, Gupta M (2021) Hardfacing studies of Ni alloys: A Critical Review. *Journal of Materials Research Technology* 10:1210–1242
7. Suraj R, Hardfacing and its effect on wear and corrosion performance of various ferrous welded mild steels, *Materials Today: Proceedings In Press* (2021) <https://doi.org/10.1016/j.matpr.2020.11.592>
8. Jilleh A, Babu NK, Thota V, Anis AL, Talari MK, Microstructural and wear investigation of high chromium white cast iron hardfacing alloys deposited on carbon steel, *Journal of Alloys and Compounds* (2020) 157472

9. Reichert M, Gerold C, Fredriksson A, Adolfsson GR, Lieberwirth H (2015) Research of iron ore grinding in a vertical-roller-mill. *Miner Eng* 73:109–115
10. Altun D, Benzer H, Aydogan N, Gerold C (2016) Operational parameters affecting the vertical roller mill performance. *Miner Eng* 103:67–71
11. Jian-Huai W, Qing-Ru C, Ya-Li K, Lynch AJ, Jin-Wu Z (2009) Grinding process within vertical roller mills: experiment and simulation. *Mining Science Technology (China)* 19(1):97–101
12. Wang H, Yu S (2017) Influence of heat treatment on microstructure and sliding wear resistance of high chromium cast iron electros slag hardfacing layer. *Surface Coatings Technology* 319:182–190
13. Buchanan VE (2009) Solidification and microstructural characterisation of iron–chromium based hardfaced coatings deposited by SMAW and electric arc spraying. *Surf Coat Technol* 203(23):3638–3646
14. Deng HX, Shi HJ, Tsuruoka S, Yu HC, Zhong B (2012) Influence of welding technique and temperature on fatigue properties of steel deposited with Co-based alloy hardfacing coating. *Int J Fatigue* 35(1):63–70
15. Amushahi MH, Ashrafizadeh F, Shamanian M (2010) Characterization of boride-rich hardfacing on carbon steel by arc spray and GMAW processes. *Surf Coat Technol* 204(16–17):2723–2728
16. Chatterjee S, Pal TK (2006) Weld procedural effect on the performance of iron based hardfacing deposits on cast iron substrate. *J Mater Process Technol* 173(1):61–69
17. Balakrishnan M, Balasubramanian V, Reddy GM (2013) Effect of hardfaced interlayer thickness on ballistic performance of armour steel welds. *Mater Des* 44:59–68
18. Kesavan D, Kamaraj M (2011) Influence of aging treatment on microstructure, wear and corrosion behavior of a nickel base hardfaced coating. *Wear* 272(1):7–17
19. Liyanage T, Fisher G, Gerlich AP, Microstructures and abrasive wear performance of PTAW deposited Ni–WC overlays using different Ni-alloy chemistries, *Wear* 274–275 (2012) 345–354
20. Guoqing C, Xuesong F, Yanhui W, Shan L, Wenlong Z (2013) Microstructure and wear properties of nickel-based surfacing deposited by plasma transferred arc welding. *Surf Coat Technol* 228:S276–S282
21. Badisch E, Kirchgaßner M (2008) Influence of welding parameters on microstructure and wear behaviour of a typical NiCrBSi hardfacing alloy reinforced with tungsten carbide. *Surf Coat Technol* 202(24):6016–6022
22. Baldrige T, Poling G, Foroozmehr E, Kovacevic R, Gupta MC (2013) Laser cladding of Inconel 690 on Inconel 600 superalloy for corrosion protection in nuclear applications. *Optics Lasers in Engineering* 51(2):180–184
23. Govardhan D, Kumar ACS, Murti KGK, Reddy GM (2012) Characterization of austenitic stainless steel friction surfaced deposit over low carbon steel. *Materials Design* 36:206–214
24. Wang Y, Gou J, Chu R, Zhen D, Liu S (2016) The effect of nano-additives containing rare earth oxides on sliding wear behavior of high chromium cast iron hardfacing alloys. *Tribol Int* 103:102–112

25. Junfeng G, You W, Wang C, Ruiqing, Chu, Saiyue, Liu (2017) Effect of rare earth oxide nano-additives on micro-mechanical properties and erosion behavior of Fe-Cr-C-B hardfacing alloys. *J Alloy Compd* 691:800–810
26. Wang J, Liu T, Zhou Y, Xing X, Liu S, Yang Y, Yang Q (2017) Effect of nitrogen alloying on the microstructure and abrasive impact wear resistance of Fe-Cr-C-Ti-Nb hardfacing alloy. *Surf Coat Technol* 309:1072–1080
27. Ali DSA, Amir M, Erdem A, Huseyin C (2018) Influence of Mo on the high temperature wear performance of NiCrBSi hardfacings. *Tribol Int* 127:288–295
28. Liu D, Liu R, Wei Y (2012) Effects of titanium additive on microstructure and wear performance of iron-based slag-free self-shielded flux-cored wire. *Surface Coatings Technology* 207:579–586
29. Zhou YF, Yang YL, Jiang YW, Yang J, Ren XJ, Yang QX (2012) Fe-24 wt.%Cr-4.1 wt.%C hardfacing alloy: Microstructure and carbide refinement mechanisms with ceria additive. *Mater Charact* 72:77–86
30. Zikin A, Antonov M, Hussainova I, Katona L, Gavrilovi A (2012) High temperature wear of cermet particle reinforced NiCrBSi hardfacings. *Tribol Int* 68:45–55
31. Wang XL, Payzant EA, Taljat B, Hubbard CR, Keiser JR, Jirinec MJ (1997) Experimental determination of the residual stresses in a spiral weld overlay tube. *Mater Sci Eng A* 232(1–2):31–38
32. Woo W, Em V, Hubbard CR, Lee HJ, Park KS (2011) Residual stress determination in a dissimilar weld overlay pipe by neutron diffraction. *Materials Science Engineering A* 528(27):8021–8027
33. Edwards L, Bouchard JP, Dutta M (2005) and, Q. D., Direct measurement of the residual stresses near a 'boat-shaped' repair in a 20 mm thick stainless steel tube butt weld. *Int J Press Vessels Pip* 82(4):288–298
34. Sachajdak A, Soma J, Szczygie I (2018) Thermal model of the Gas Metal Arc Welding hardfacing process. *Appl Therm Eng* 141:378–385
35. Yang QX, Yao M, Park JK (2004) Numerical simulations and measurements of temperature and stress field in medium-high carbon steel specimen after hard-face-welding. *Comput Mater Sci* 29(1):37–42
36. Jiang WC, Wang BY, Gong JM, Tu ST (2011) Finite element analysis of the effect of welding heat input and layer number on residual stress in repair welds for a stainless steel clad plate. *Materials Design* 32(5):2851–2857
37. Jiang W, Xu XP, Gong JM, Tu ST (2012) Influence of repair length on residual stress in the repair weld of a clad plate. *Nucl Eng Des* 246:211–219
38. Ma L, Huang C, Jiang J, Hui R, Xie Y, Liu ZS (2013) Cracks formation and residual stress in chromium carbide overlays. *Eng Fail Anal* 31:320–337
39. Lv S, Song J, Wang H, Yang S (2009) Temperature field and flow field during tungsten inert gas bead welding of copper alloy onto steel. *Materials Science Engineering A* 499(1–2):347–351

40. Ru-Feng L, Chin-Cheng, Huang (2013) Welding residual stress analysis for weld overlay on a BWR feedwater nozzle. *Nucl Eng Des* 256:291–303
41. Klobčar D, Tušek J, Taljat B (2004) Finite element modeling of GTA weld surfacing applied to hot-work tooling. *Comput Mater Sci* 31(3–4):368–378
42. Kim KS, Lee HJ, Lee BS, Jung IC, Park KS (2009) Residual stress analysis of an Overlay weld and a repair weld on the dissimilar Butt weld. *Nuclear Engineering Design* 239(12):2771–2777
43. Wu AP, Ren JL, Peng ZS, Murakawa H, Ueda Y (2000) Numerical simulation for the residual stresses of Stellite hard-facing on carbon steel. *J Mater Process Technol* 101(1–3):70–75
44. Winczek J (2012) Modelling of heat affected zone in cylindrical steel elements surfaced by welding. *Appl Math Model* 36(4):1514–1528
45. Winczek J (2011) New approach to modeling of temperature field in surfaced steel elements. *International Journal of Heat Mass Transfer* 54(21–22):4702–4709
46. Parkitny R, Winczek J (2013) Analytical solution of temporary temperature field in half-infinite body caused by moving tilted volumetric heat source. *International Journal of Heat Mass Transfer* 60:469–479
47. ESI Group. SYSWELD 2010 reference manual. Digital Version 2010
48. ESI Group. SYSWORLD 2010 technical description of capabilities. Digital Version 2010.
49. J. Goldak, A. Chakravarti, M. Bibby, A new finite element model for welding heat sources, *Metallurgical Transactions B* 15(2) (1984) 299–305.
50. J. Goldak, M. Bibby, J. Moore, R. House, B. Patel, Computer modeling of heat flow in welds, *Metallurgical Transactions B* 17(3) (1986) 587–600.
51. P.-H. Chang, T.-L. Teng, Numerical and experimental investigations on the residual stresses of the butt-welded joints, *Computational Materials Science* 29(4) (2004) 511–522.
52. ASTM A36. Standard Specification for Carbon Structural Steel, 2008.
53. V. Kumlytis, A.V. Valiulis, O. Ernajus, The Influence of Temperature-Time Parameter of Welded Joints Thermal Treatment on Strength-Related Characteristics of Chromium-Molybdenum and Low-Alloy Manganese Steels, *Materials Science* 13(2) (2007) 123–126.
54. H. Yan, Numerical simulation about butt-welding deformation [Master dissertation], Hefei University of Technology, Hefei, 2009, [in Chinese].
55. A.E.D. Silva, I.N.R.D. Melo, I.P. Pinheiro, L.R.D. Silva, Characterisation and machinability of high chromium hardened white cast iron with and without the addition of niobium, *Wear* 460–461 (2020) 203463.
56. T. S, M. S, Thermo-Calc, JMatPro and their applications, *Proceeding of 26th material seminar*, Materials Science Society of Japan, Japan, 2002, pp. 117–123.
57. N. Saunders, U.K.Z. Guo, X. Li, A.P. Miodownik, J.-P. Schillé, Using JMatPro to model materials properties and behavior, *JOM* 55 (2003) 60–65.
58. J.R. Davis, *ASM Specialty Handbook: Cast Irons*, ASM International, Materials Park, OH, 1996.

59. D. Radaj, Heat effects of welding: temperature field, residual stress and distortion, Springer Verlag Publishing, Berlin Heidelberg, 1992.
60. A.S. Aloraier, S. Joshi, Residual stresses in flux cored arc welding process in bead-on-plate specimens, Materials Science & Engineering: A 534 (2012) 13–21.
61. D. Dean, M. Hidekazu, Prediction of welding residual stress in multi-pass butt-welded modified 9Cr–1Mo steel pipe considering phase transformation effects, Computational Materials Science 37(3) (2006) 209–219.
62. C. Heinze, C. Schwenk, M. Rethmeier, Numerical calculation of residual stress development of multi-pass gas metal arc welding, Materials & Design 72 (2012) 12–19.

Tables

Due to technical limitations, tables are only available as a download in the Supplemental Files section.

Figures



Figure 1

Surface cracking of hardfacing layer



Figure 2

Failure modes of grinding roller: (a) roller fracture in the mill; (b) hardfacing layers peeling off

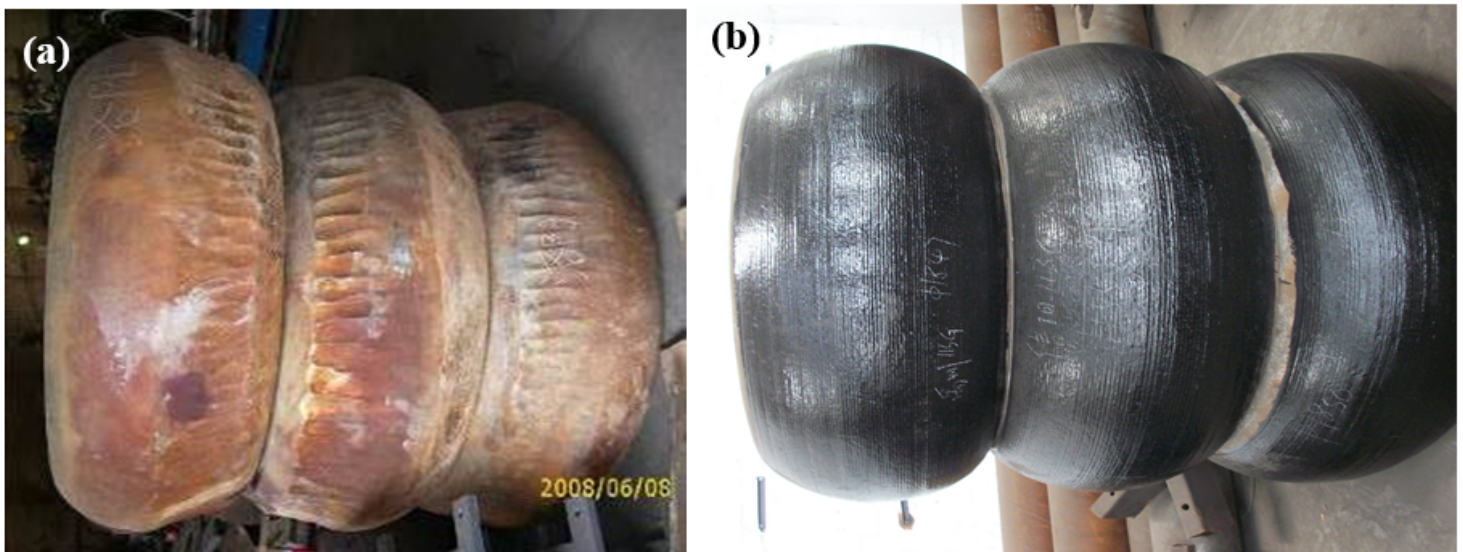


Figure 3

The off-line hardfacing for grinding roller: (a) before hardfacing, (b) after hardfacing

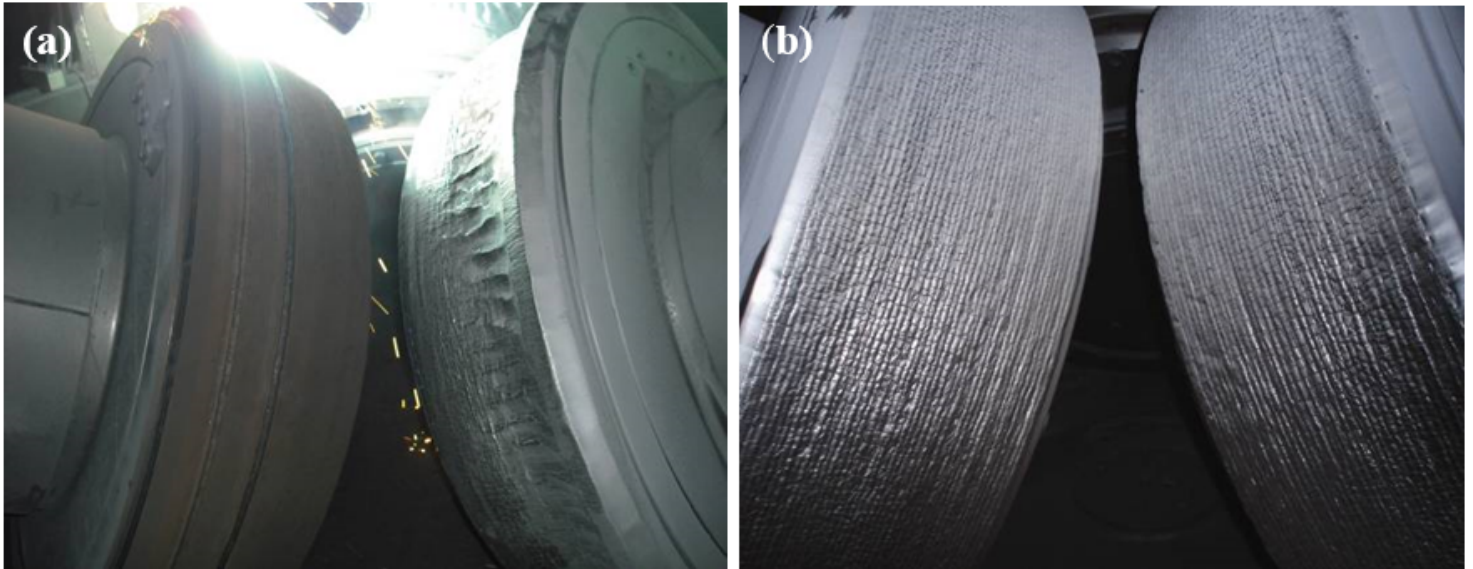


Figure 4

The on-line hardfacing for LM grinding roller: (a) before hardfacing, (b) after hardfacing

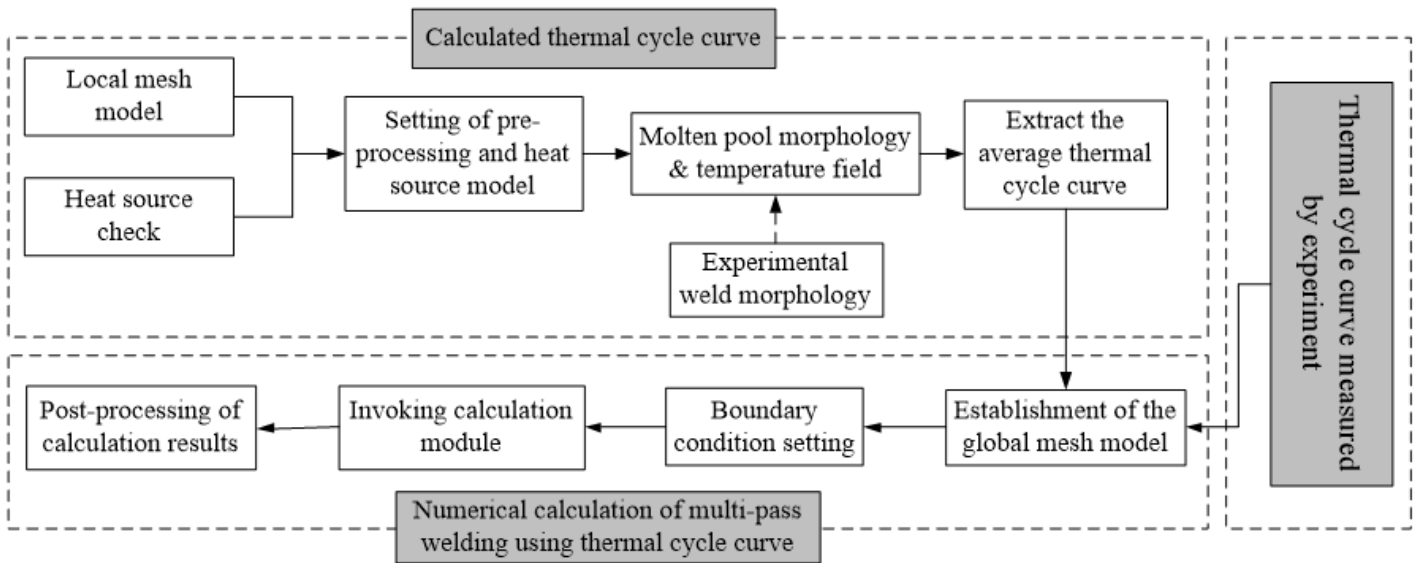


Figure 5

The calculation workflow for multi-pass welding using thermal cycle method

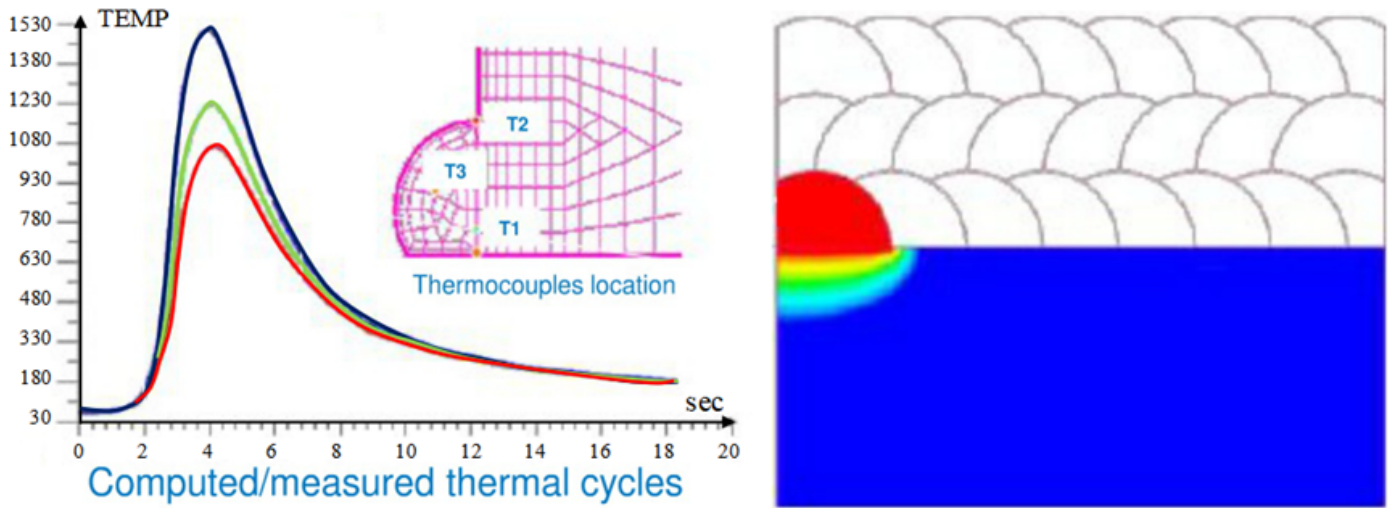


Figure 6

The surfacing welding simulation using imposed thermal cycles method

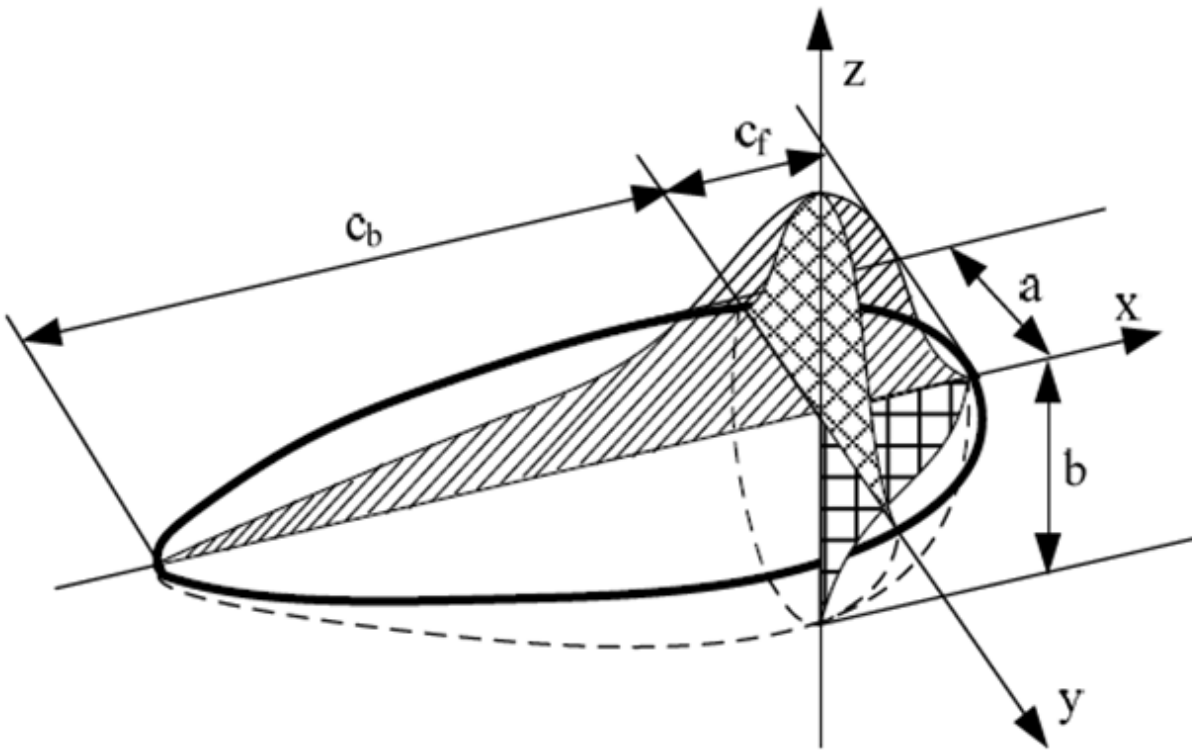


Figure 7

Double ellipsoid heat source model

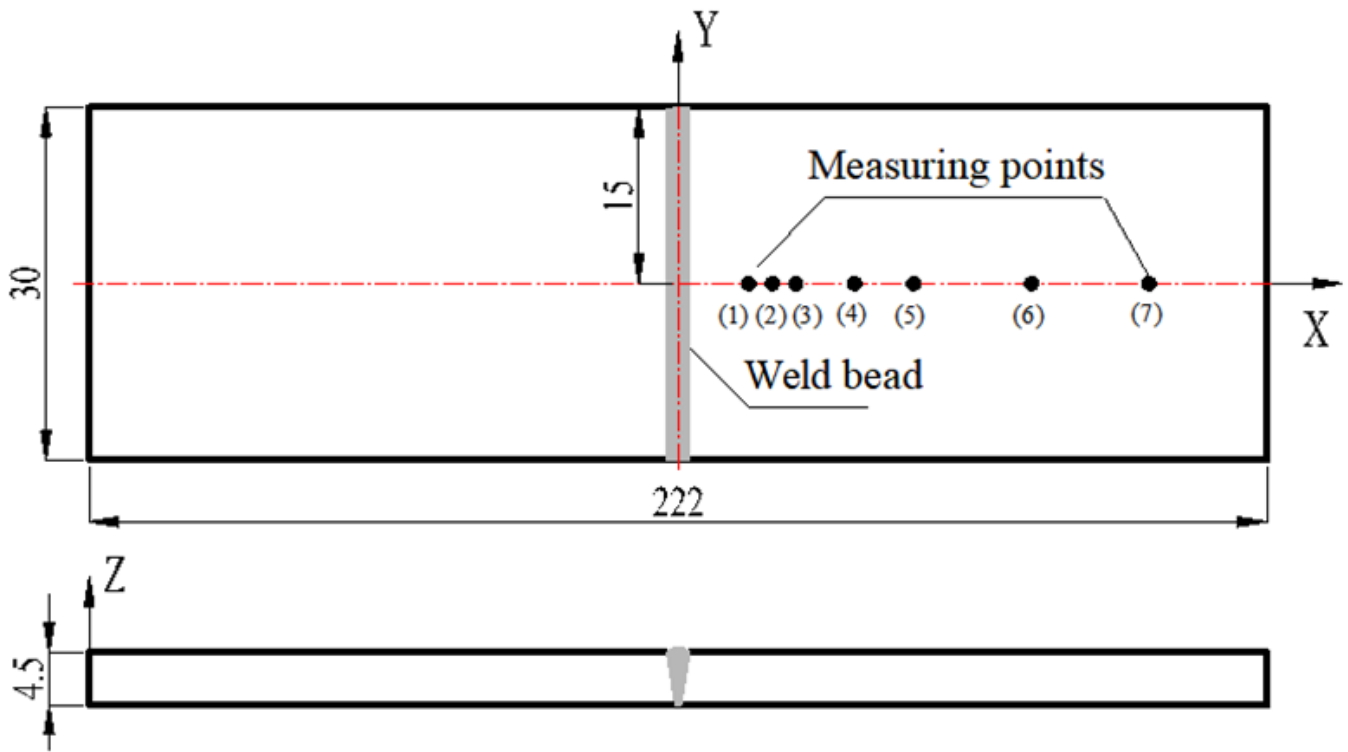


Figure 8

The specimen and measuring points

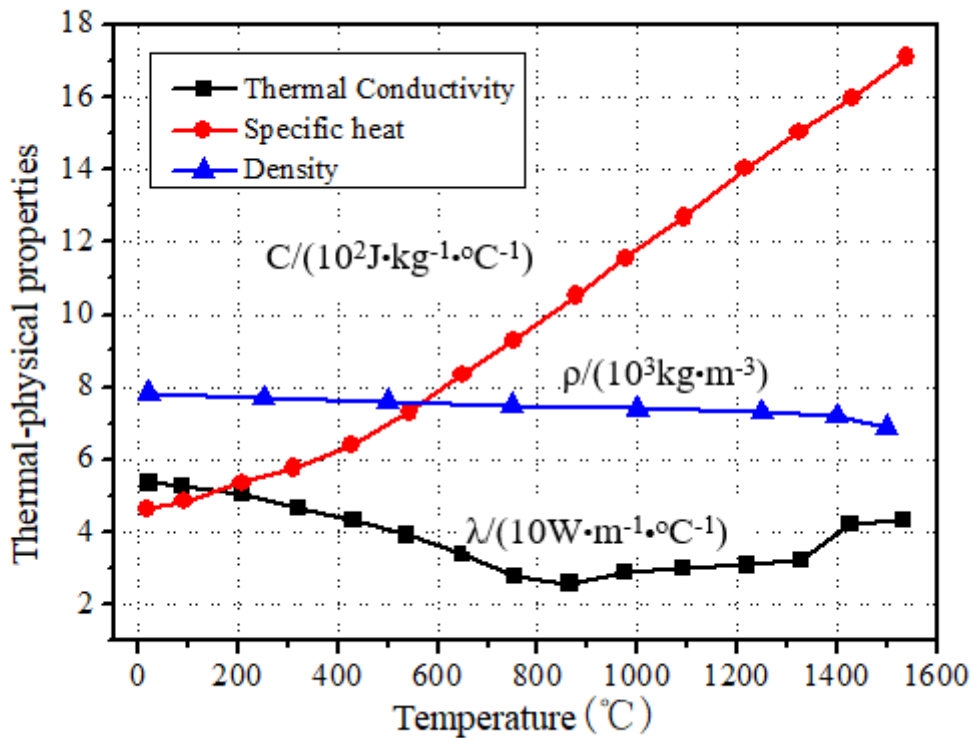


Figure 9

Temperature-dependent thermal physical properties of A36

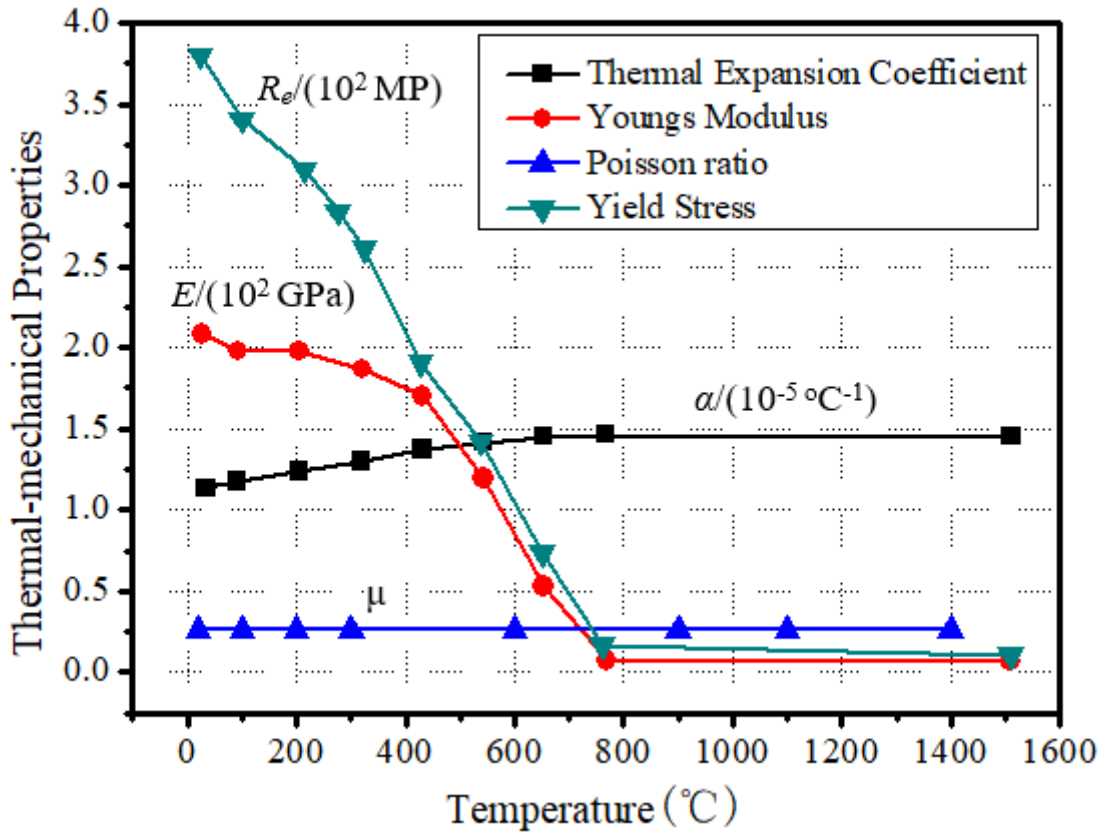


Figure 10

Temperature-dependent mechanical properties of A36

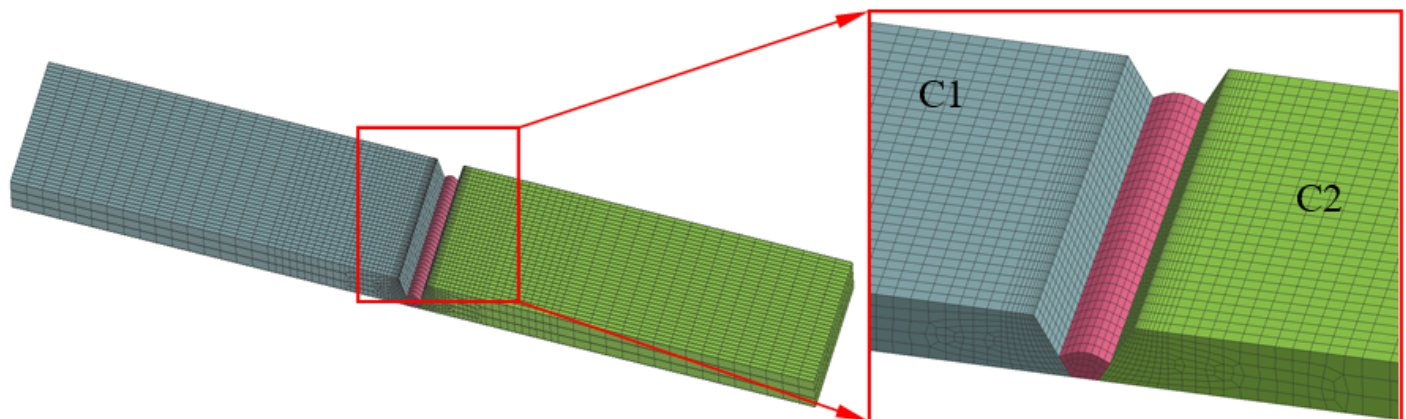


Figure 11

The local mesh model for V-groove butt welded joint

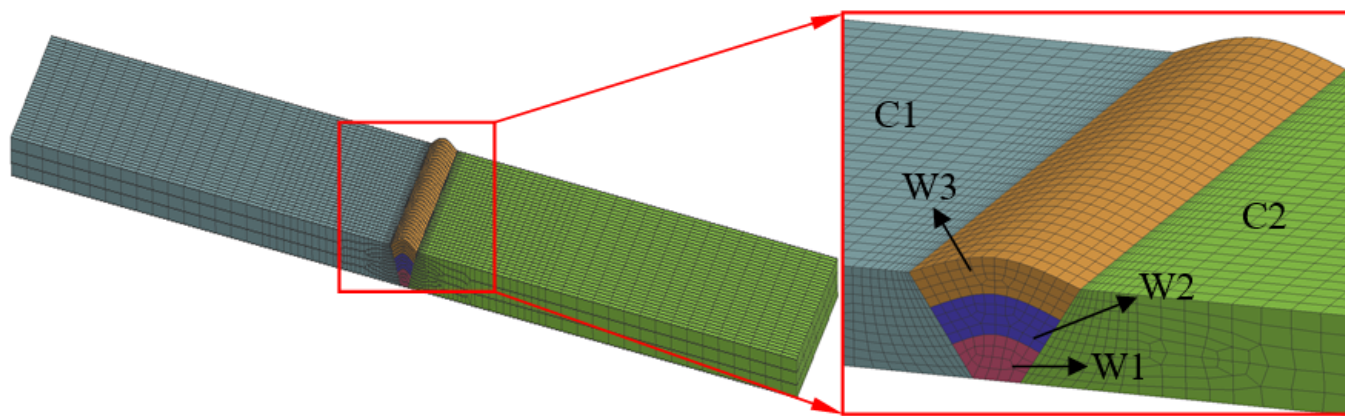


Figure 12

The global mesh model for V-groove butt welded joint

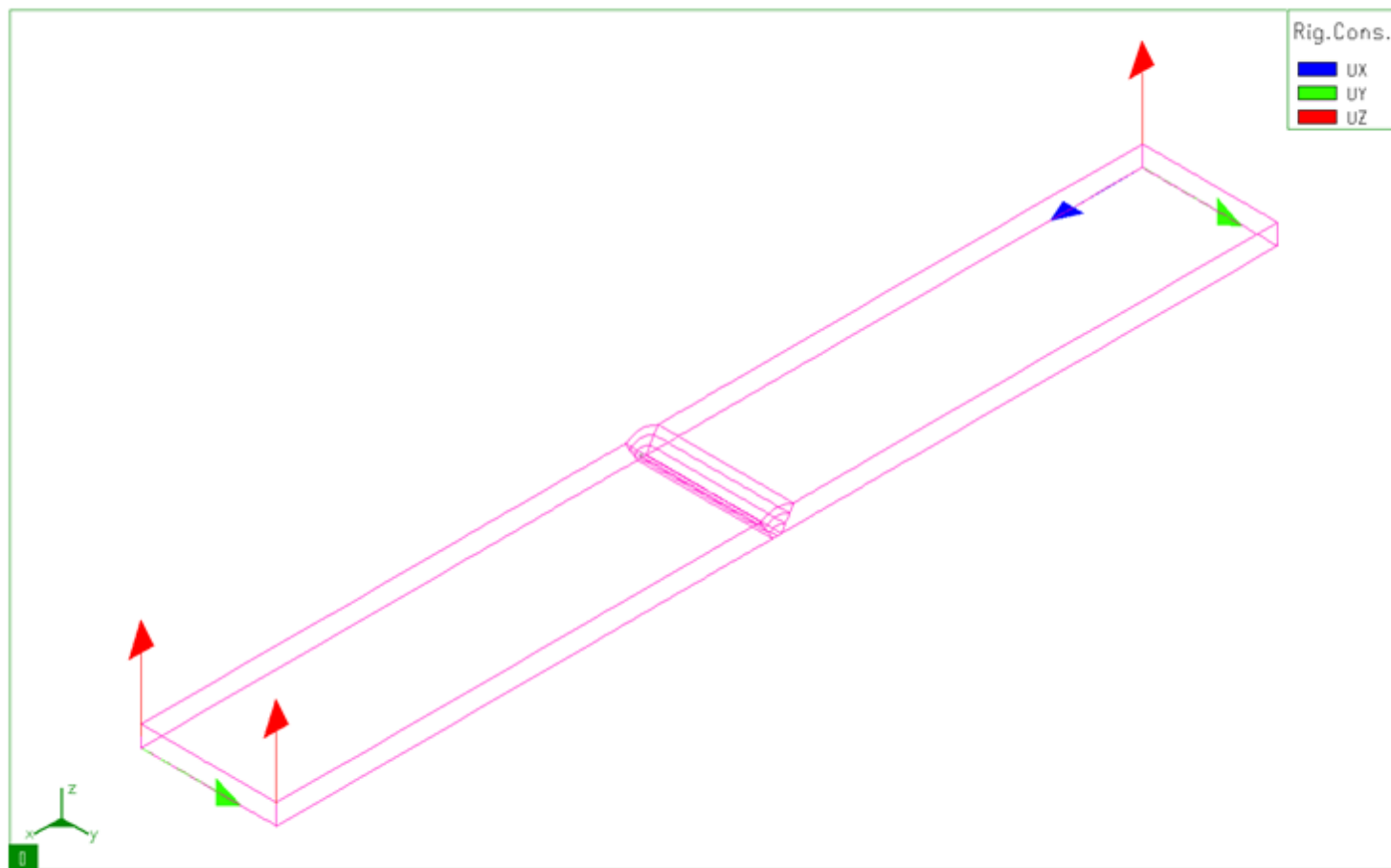


Figure 13

The constraint conditions of the model for V-groove butt welded joint

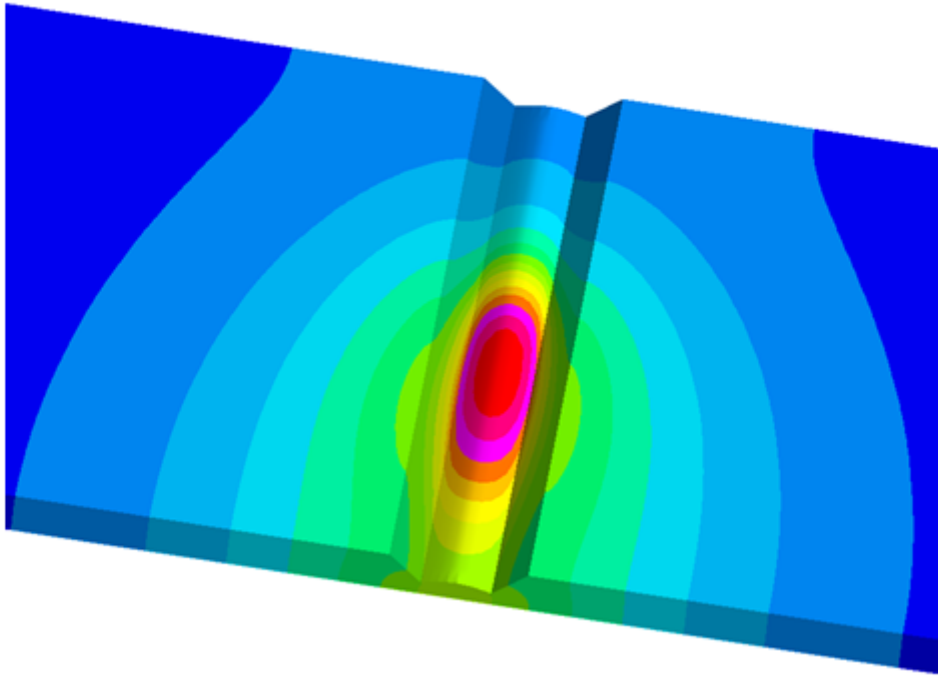


Figure 14

The steady-state temperature field of weld zone

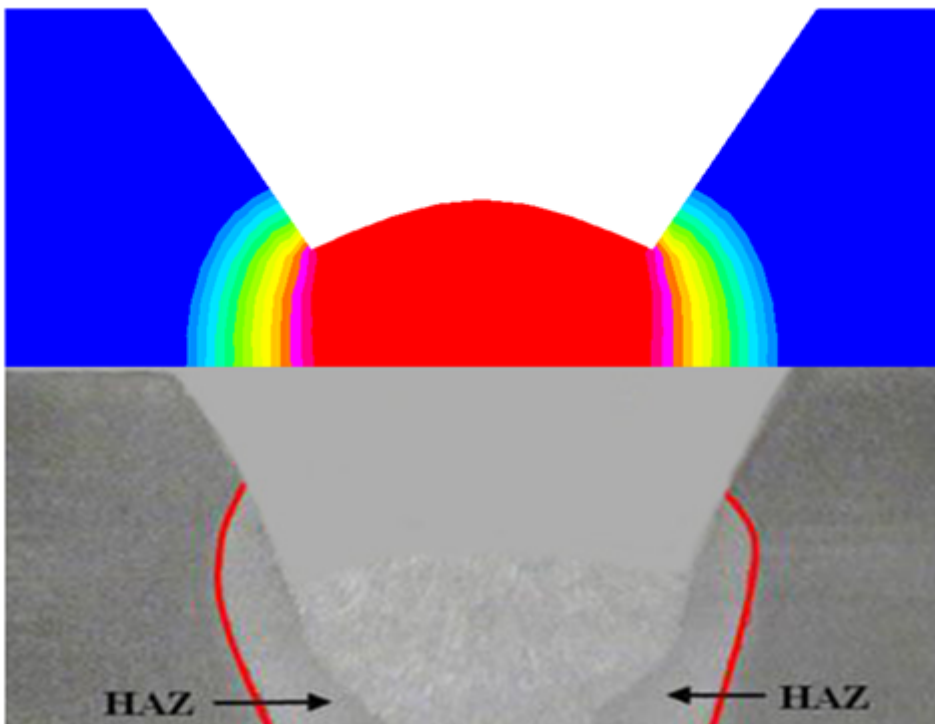


Figure 15

Molten pool shape comparison between experiment and simulation

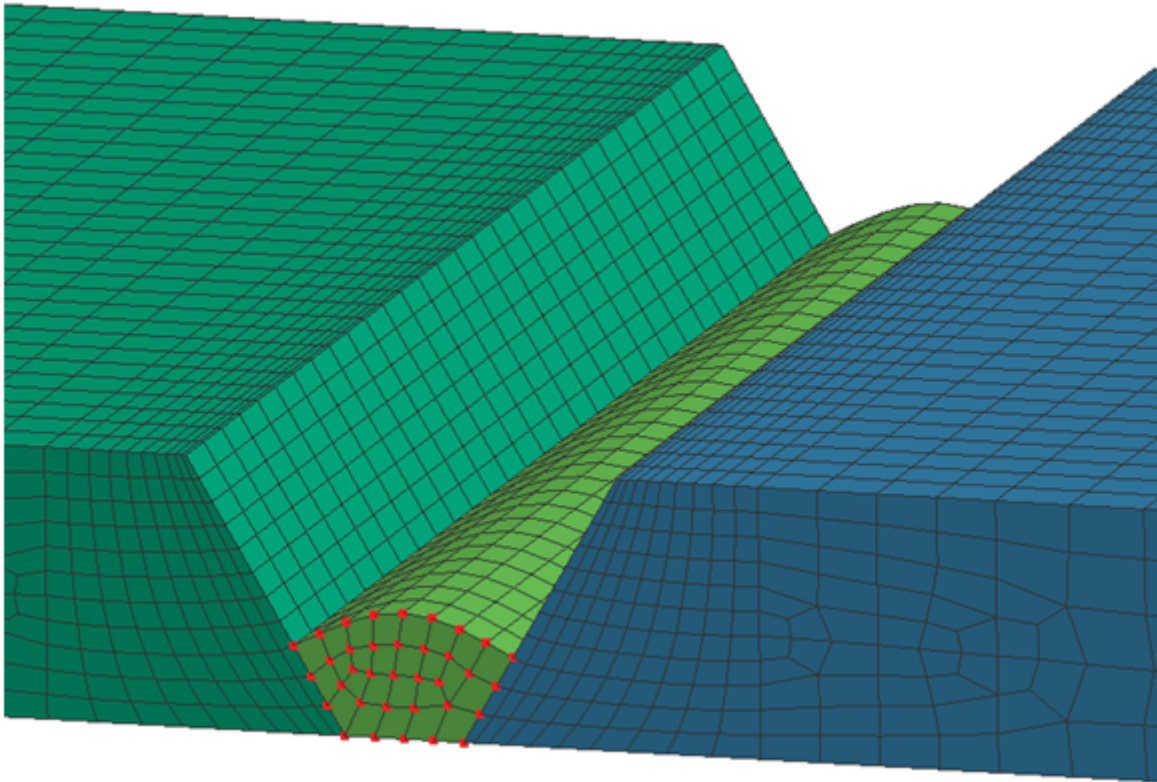


Figure 16

The nodes in the cross-section of weld bead

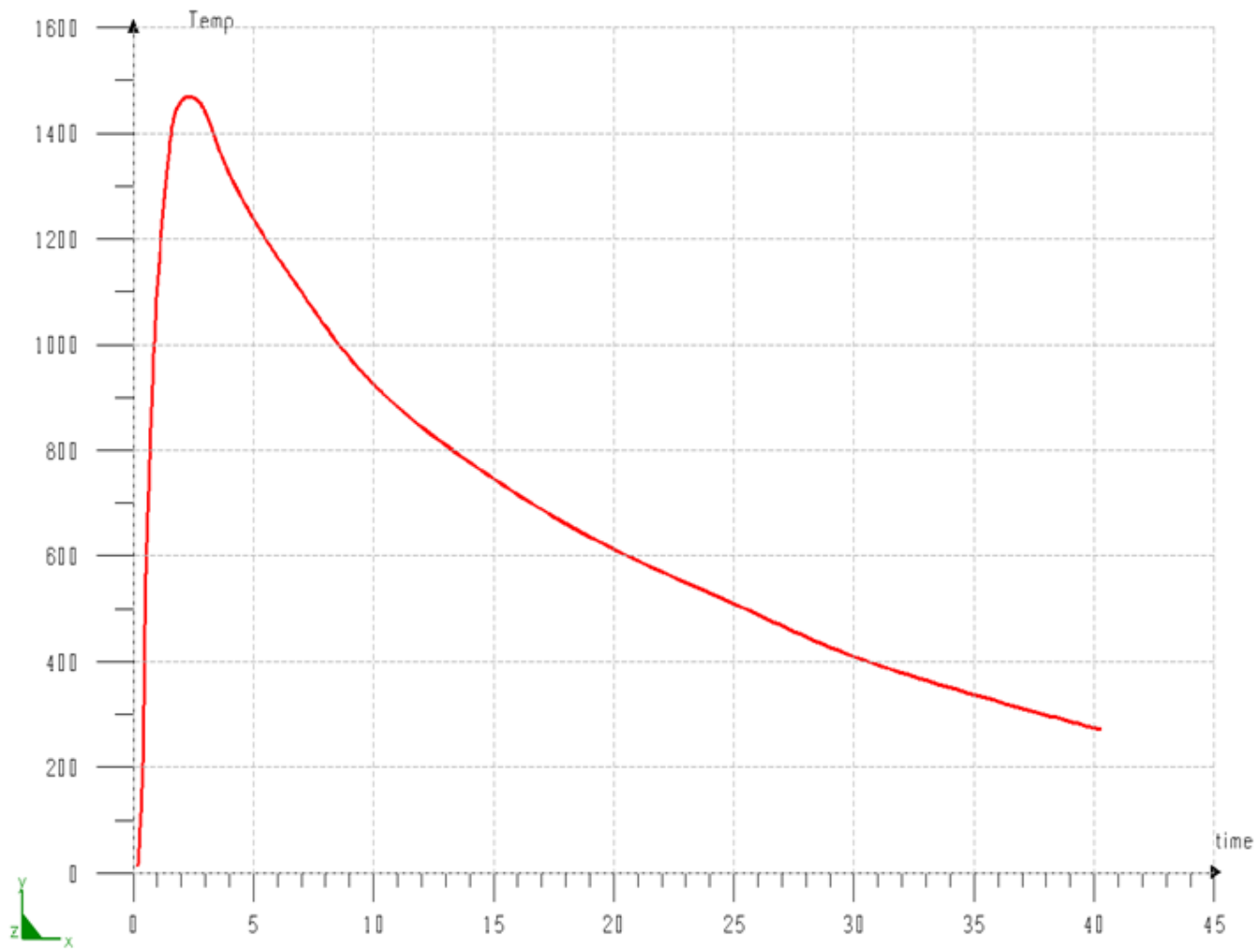


Figure 17

Average thermal cycle curve of the butt joint in the weld bead

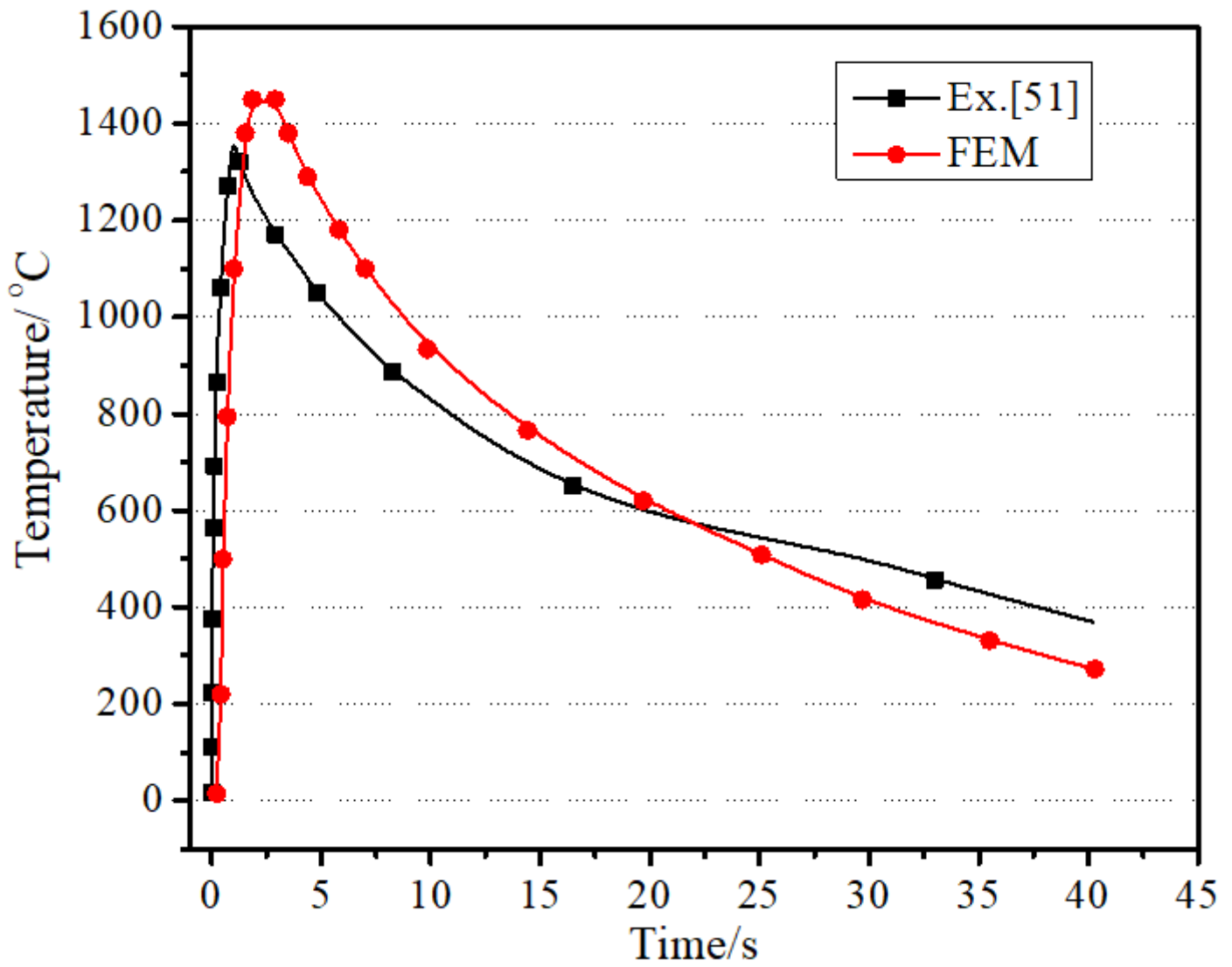


Figure 18

Comparison between experimental and numerical thermal cycle curves

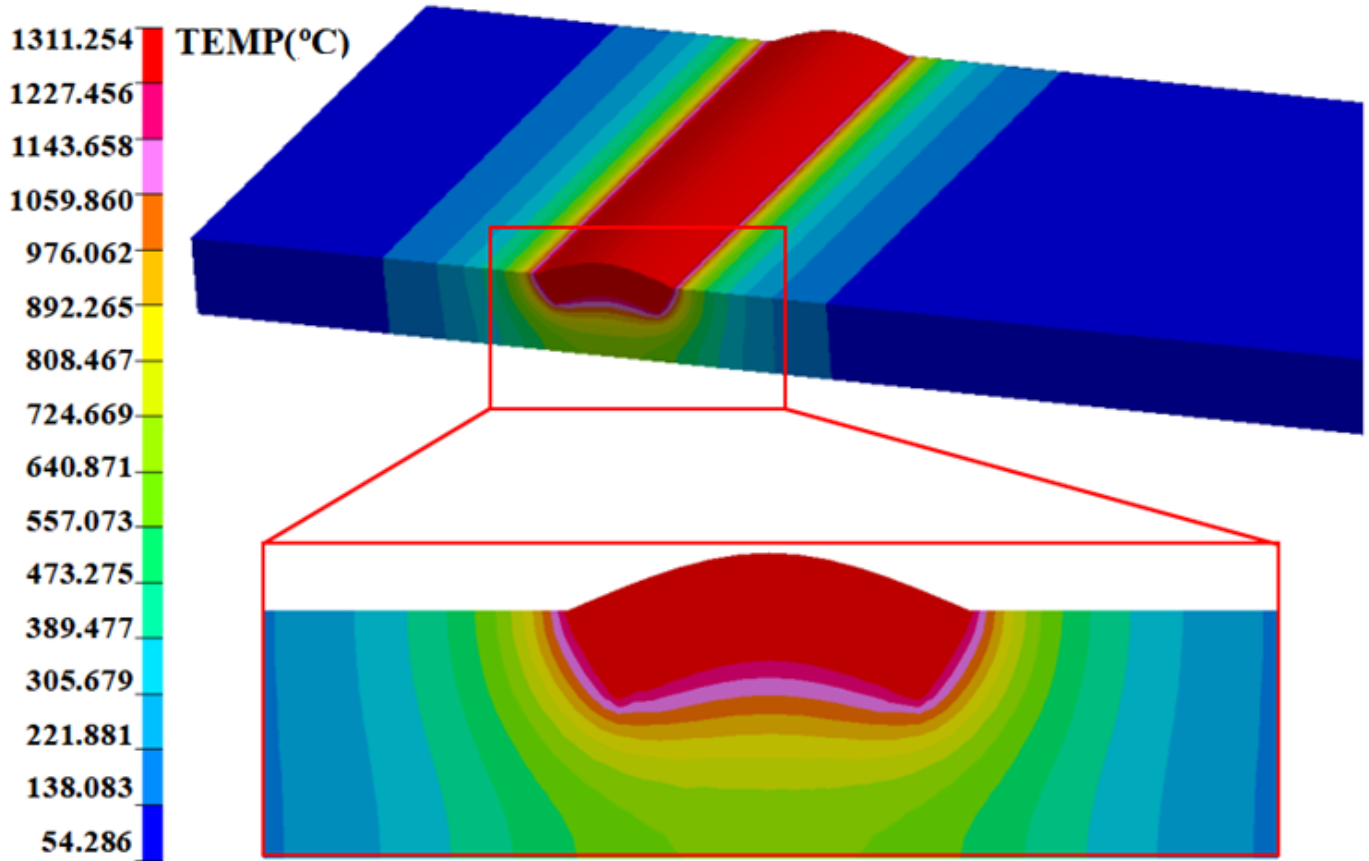


Figure 19

Temperature field of the third pass welding at $t=661.34$ s

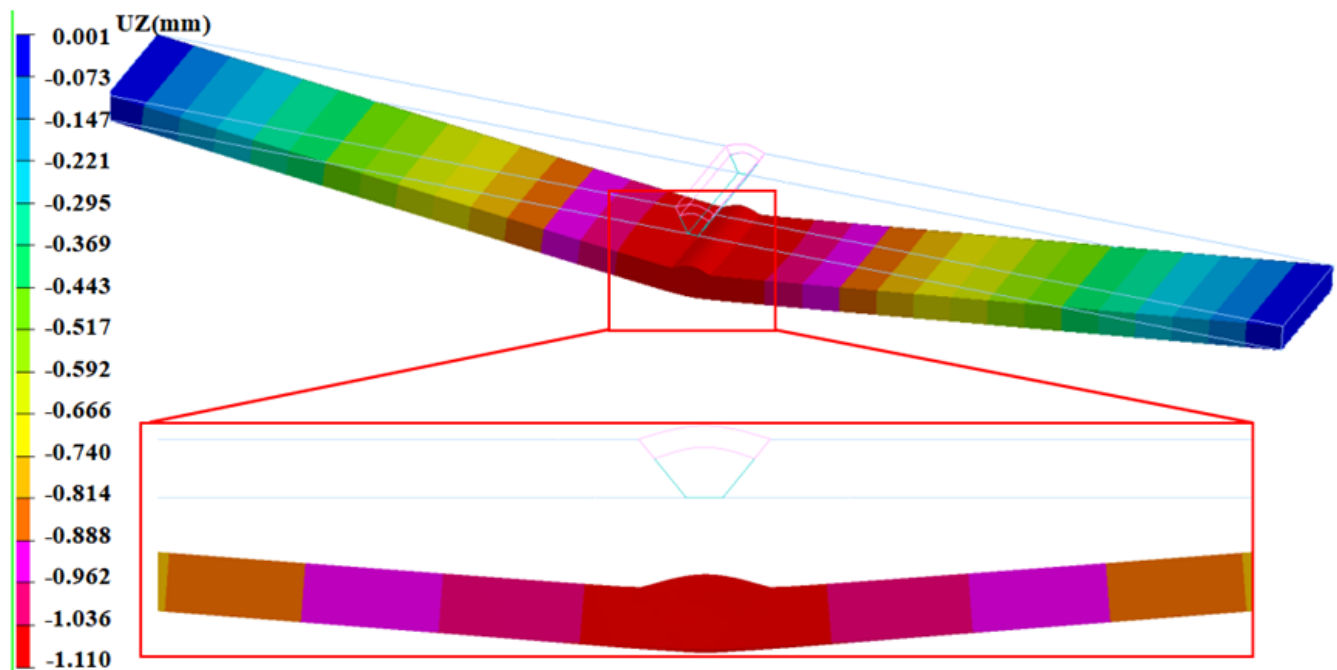


Figure 20

Angular distortions after the third welding pass

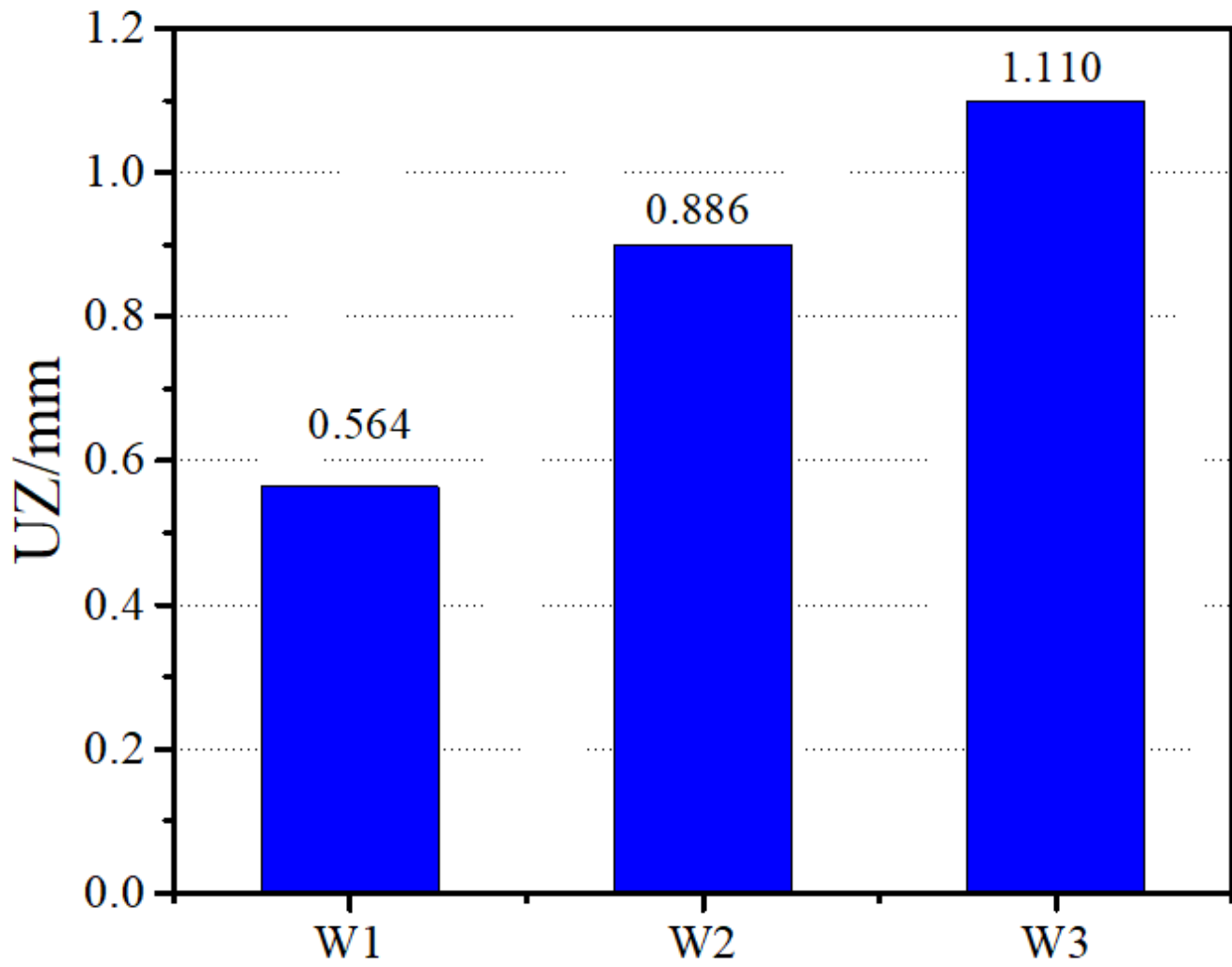


Figure 21

Angular distortions after the third welding pass

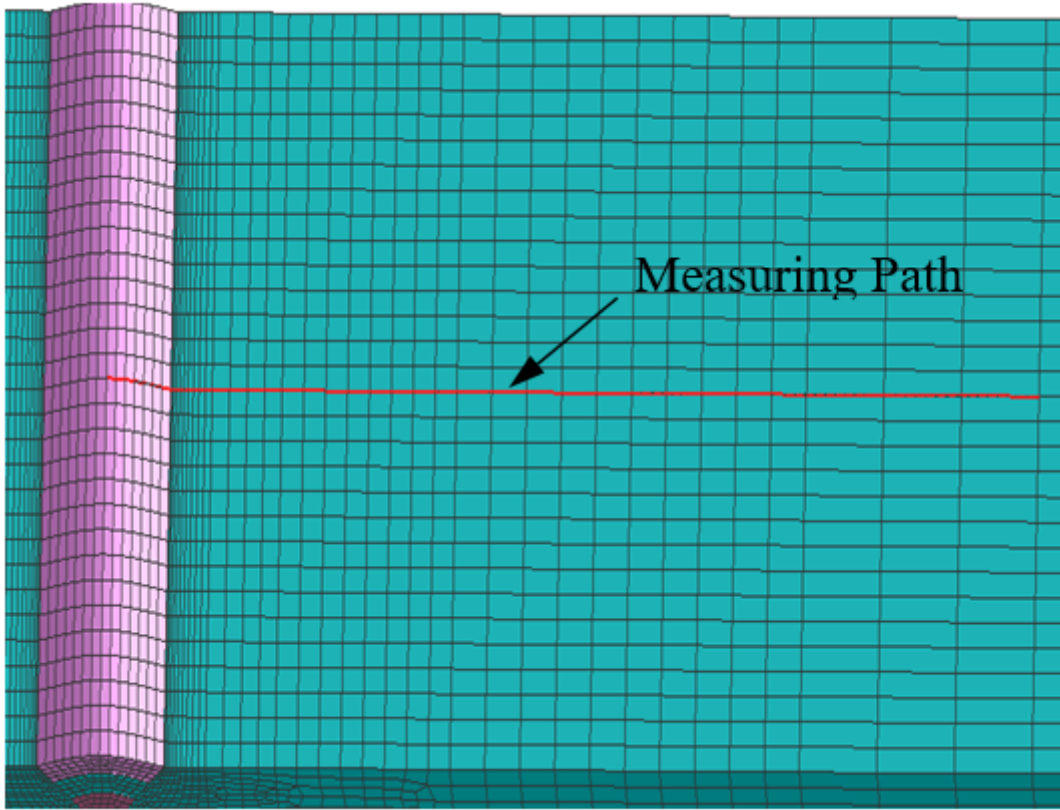


Figure 22

Measuring path for residual stresses

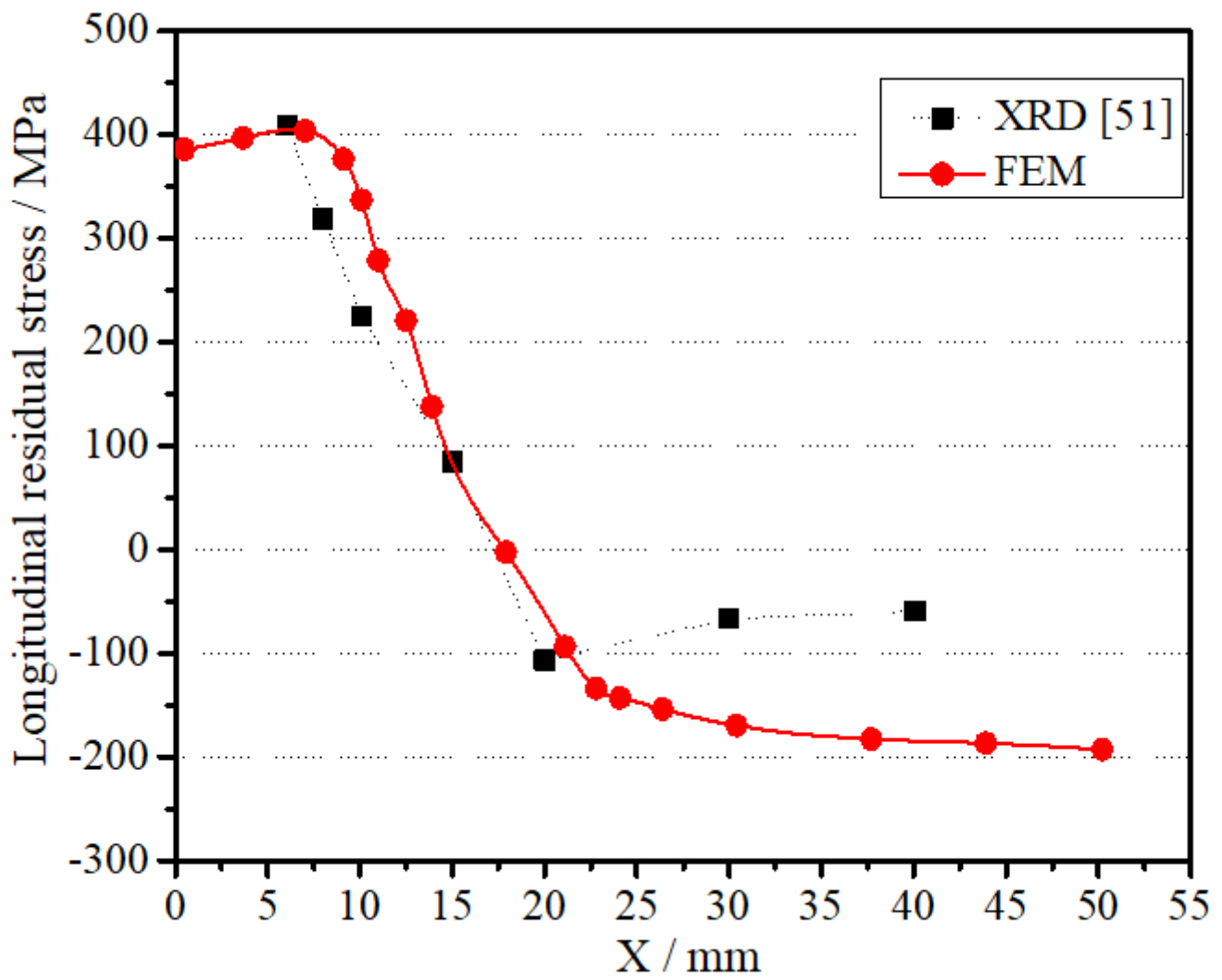


Figure 23

Comparison of longitudinal residual stresses obtained by experiment and numerical simulation

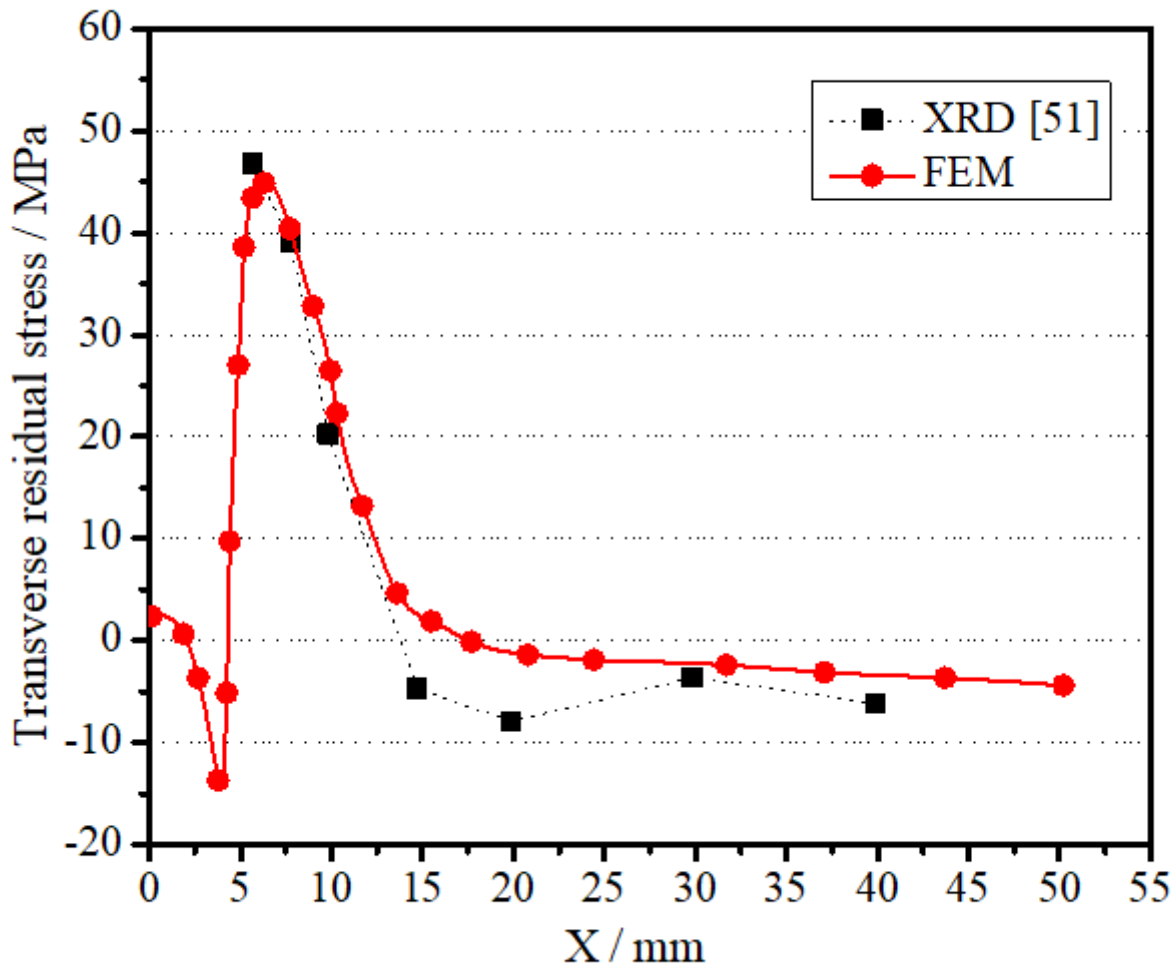


Figure 24

Comparison of longitudinal residual stresses obtained by experiment and numerical simulation



Figure 25

The HRM 2800 grinding roller with damage: (a) before gouging; (b) after gouging

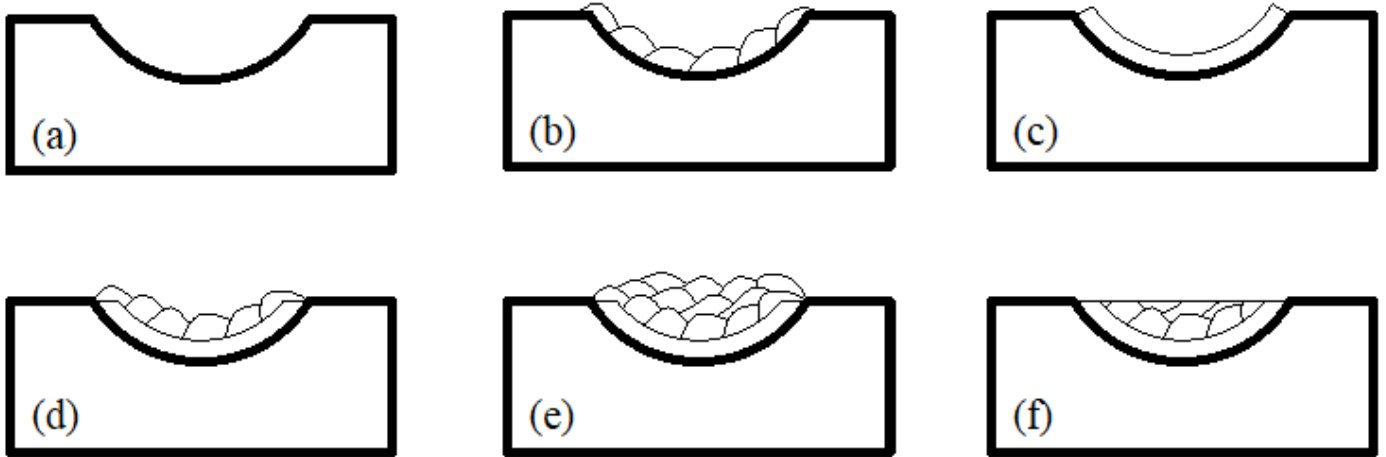


Figure 26

The hardfacing remanufacturing process for worn-out grinding roller: (a) gouging and grinding, (b) applying the buttering layer, (c) machining half of the buttering layer, (d) applying the tempering layer, (e) filling the rest of the cavity and (f) grinding the capping layer



Figure 27

The grinding roller under hardfacing

	Wt %
Fe	100.0
Al	0.0
Ni	0.0
Ti	0.0
Mo	0.0
Cr	0.0
Cu	0.0
Mg	0.0
Mn	0.0
Nb	0.0
Si	0.0
Ta	0.0
V	0.0
C	0.0
N	0.0
P	0.0
S	0.0

C equivalent: 0.0

Cast Iron

Thermodynamic Properties:

Solidification:

Mechanical Properties:

Phase transformation:

Figure 28

The calculation model of JMatPro for cast iron

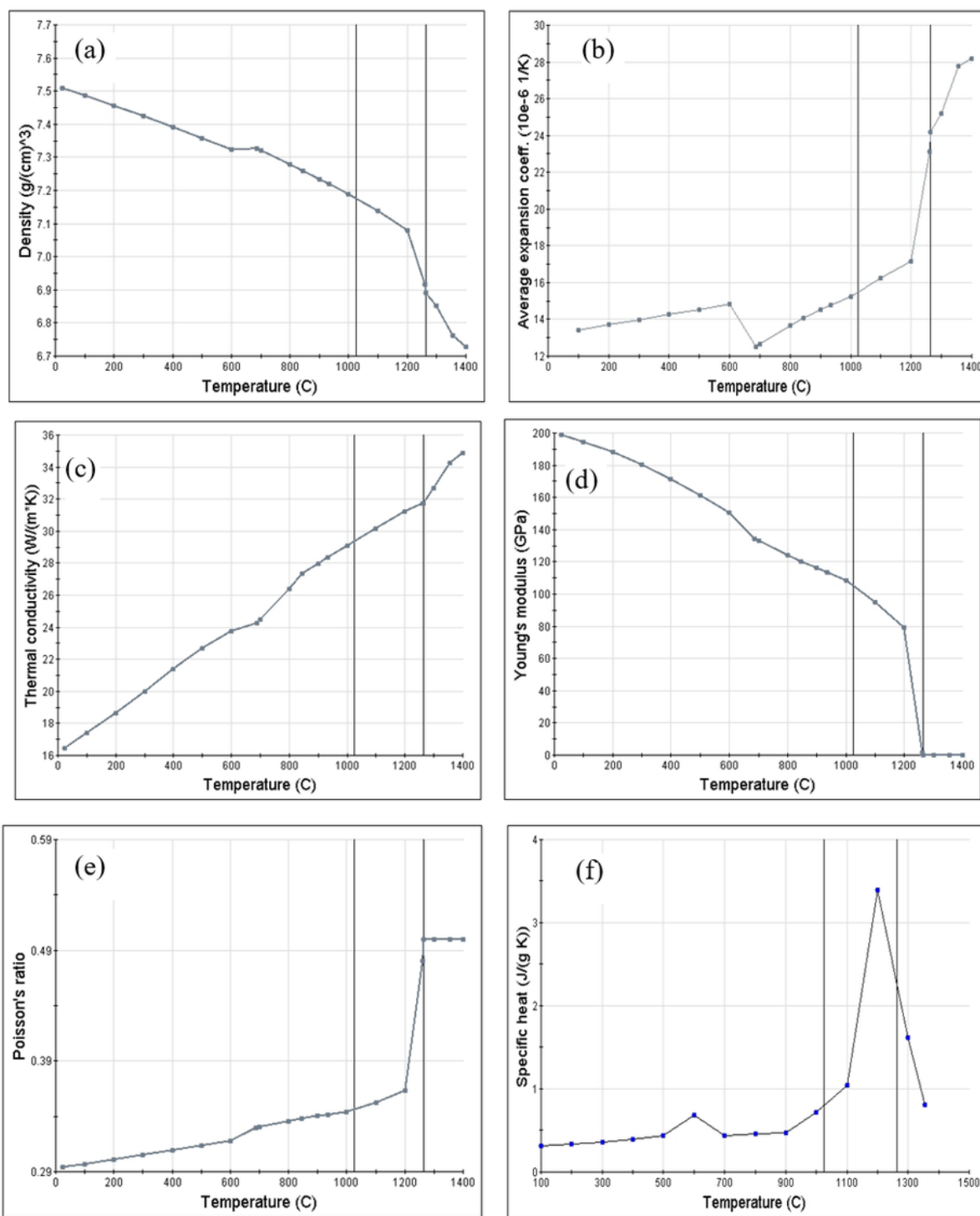


Figure 29

Temperature-dependent material properties of KmTBcr26: (a) Density; (b) Thermal expansion coeff.; (c) Thermal conductivity; (d) Young's modulus; (e) Poisson's ratio; (f) Specific heat

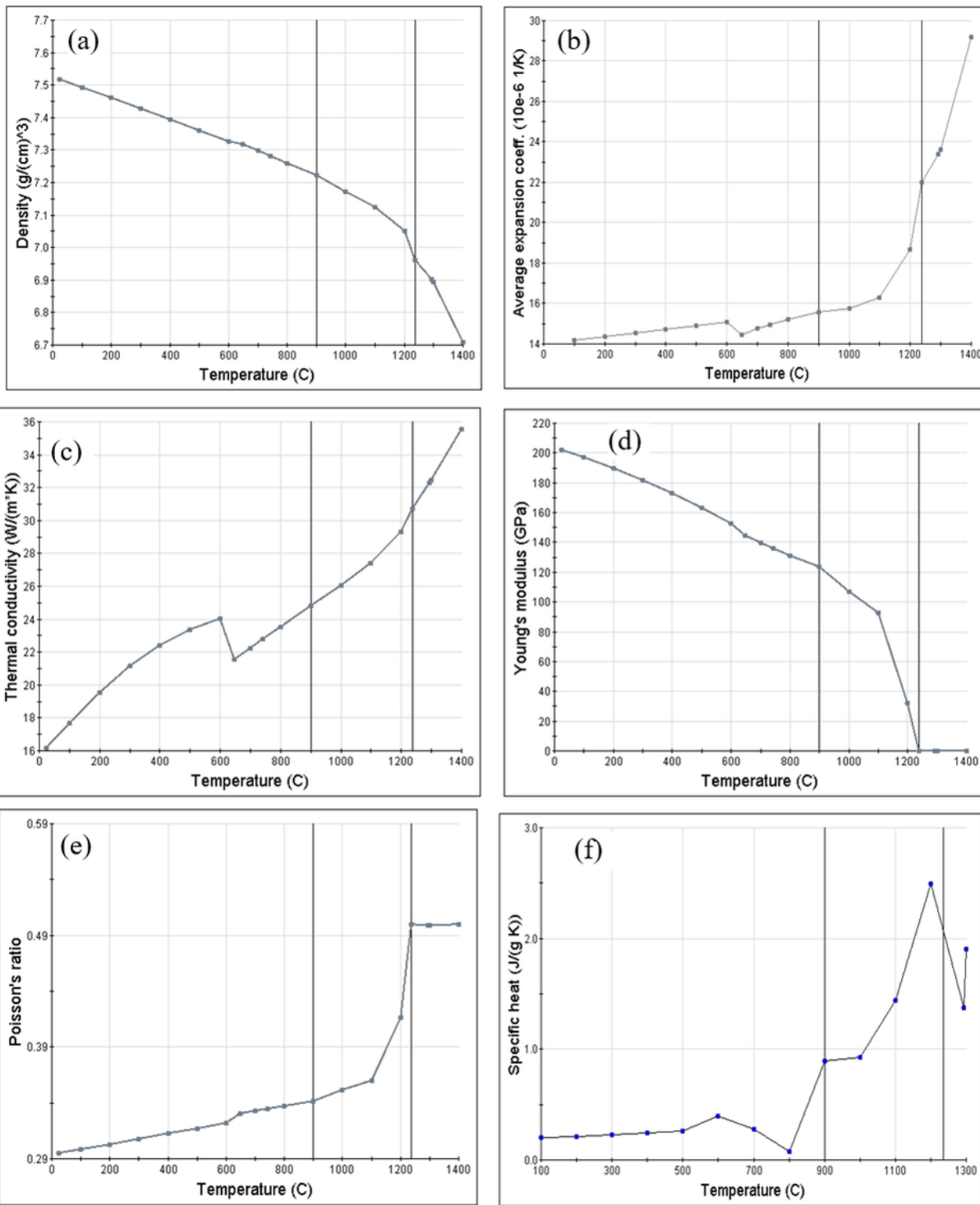


Figure 30

Temperature-dependent material properties of ARCFW9024: (a) Density; (b) Thermal expansion coeff.; (c) Thermal conductivity; (d) Young's modulus; (e) Poisson's ratio; (f) Specific heat

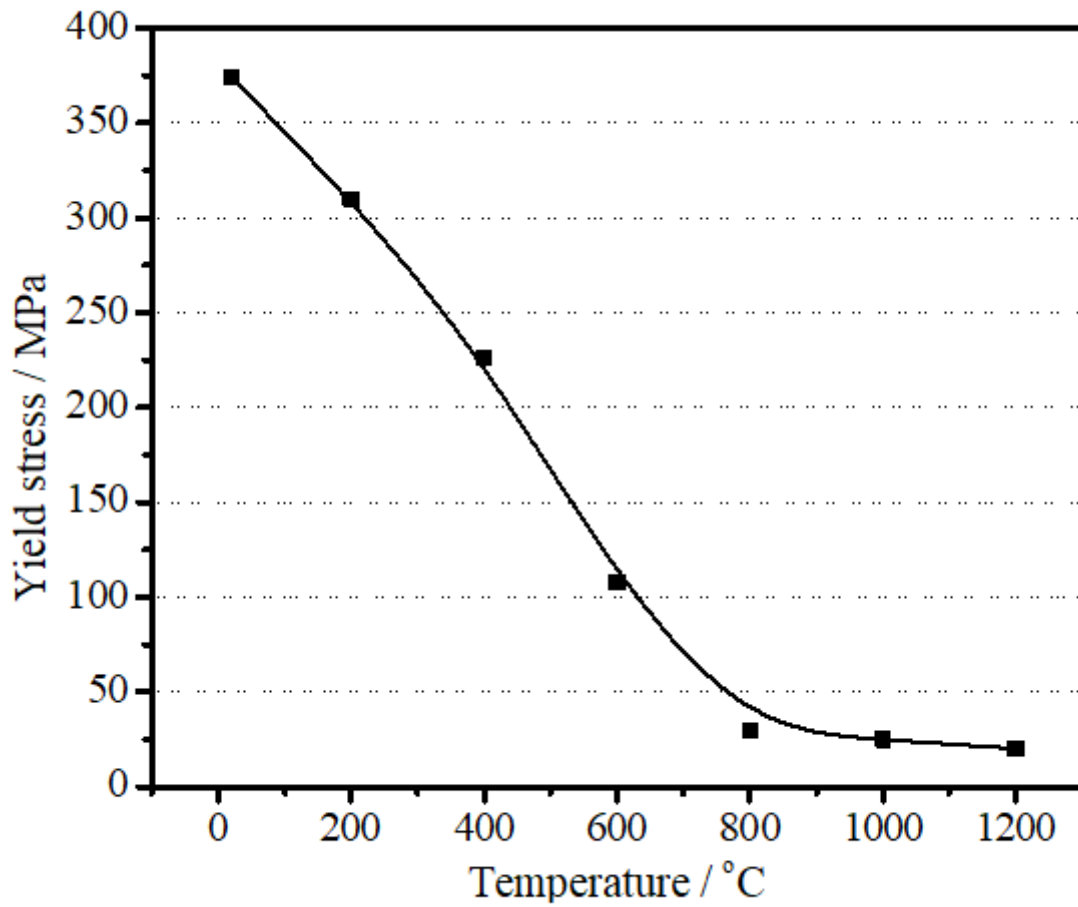


Figure 31

Temperature-dependent yield stress of High chromium cast iron

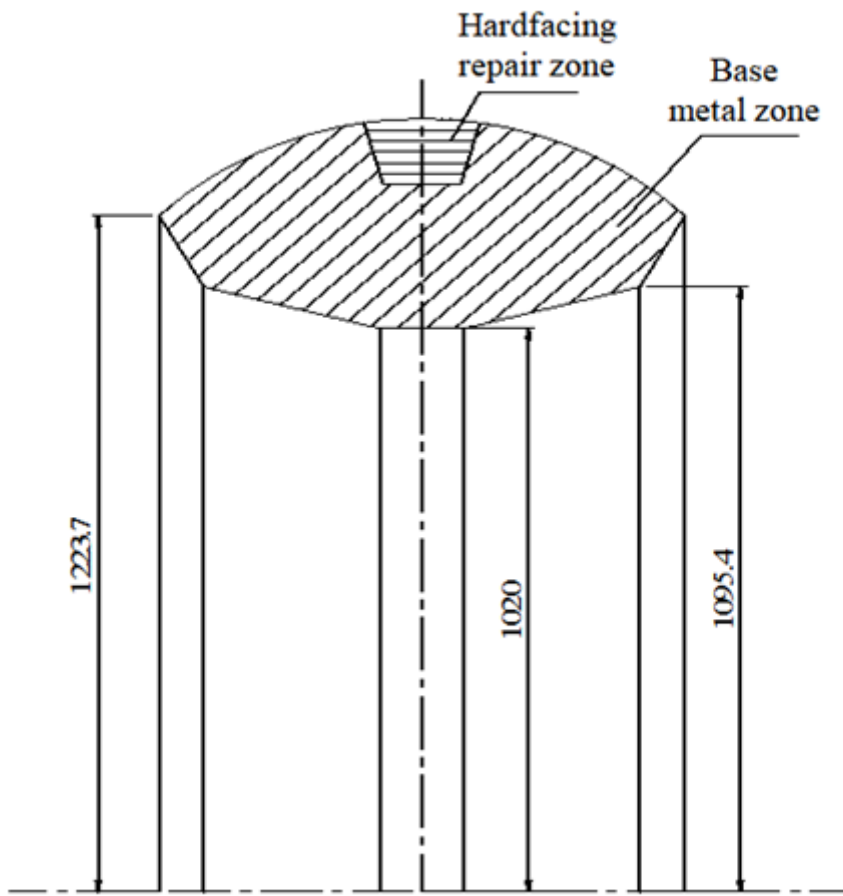


Figure 32

Geometric size of global model for hardfacing remanufacturing (unit: mm)

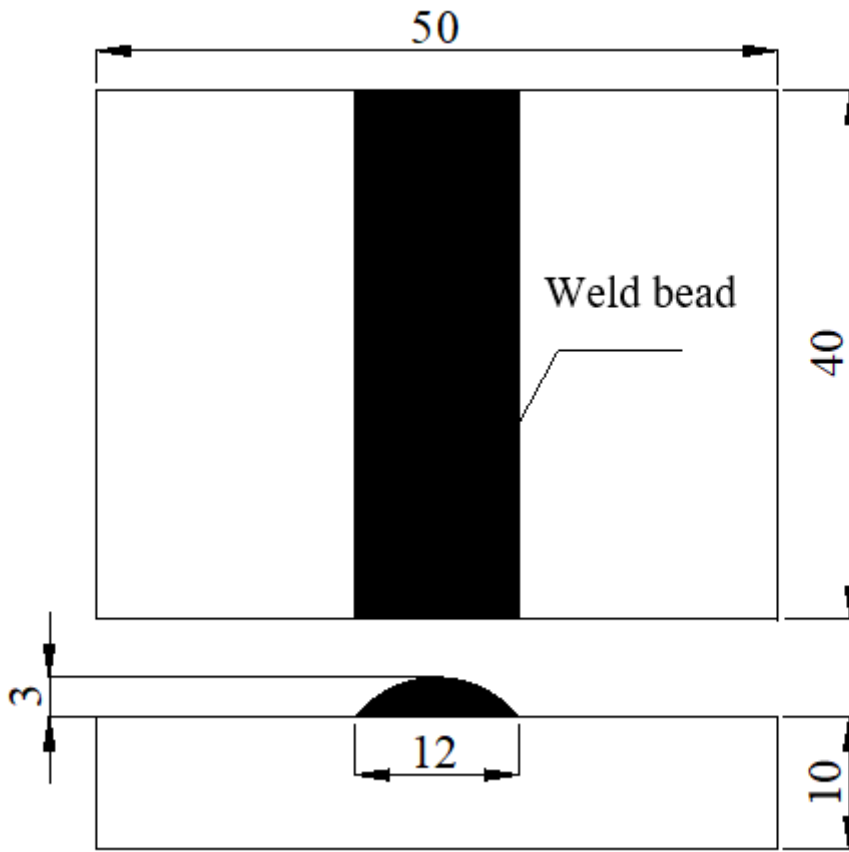


Figure 33

Geometric size of local model for heat source fitting (unit: mm)

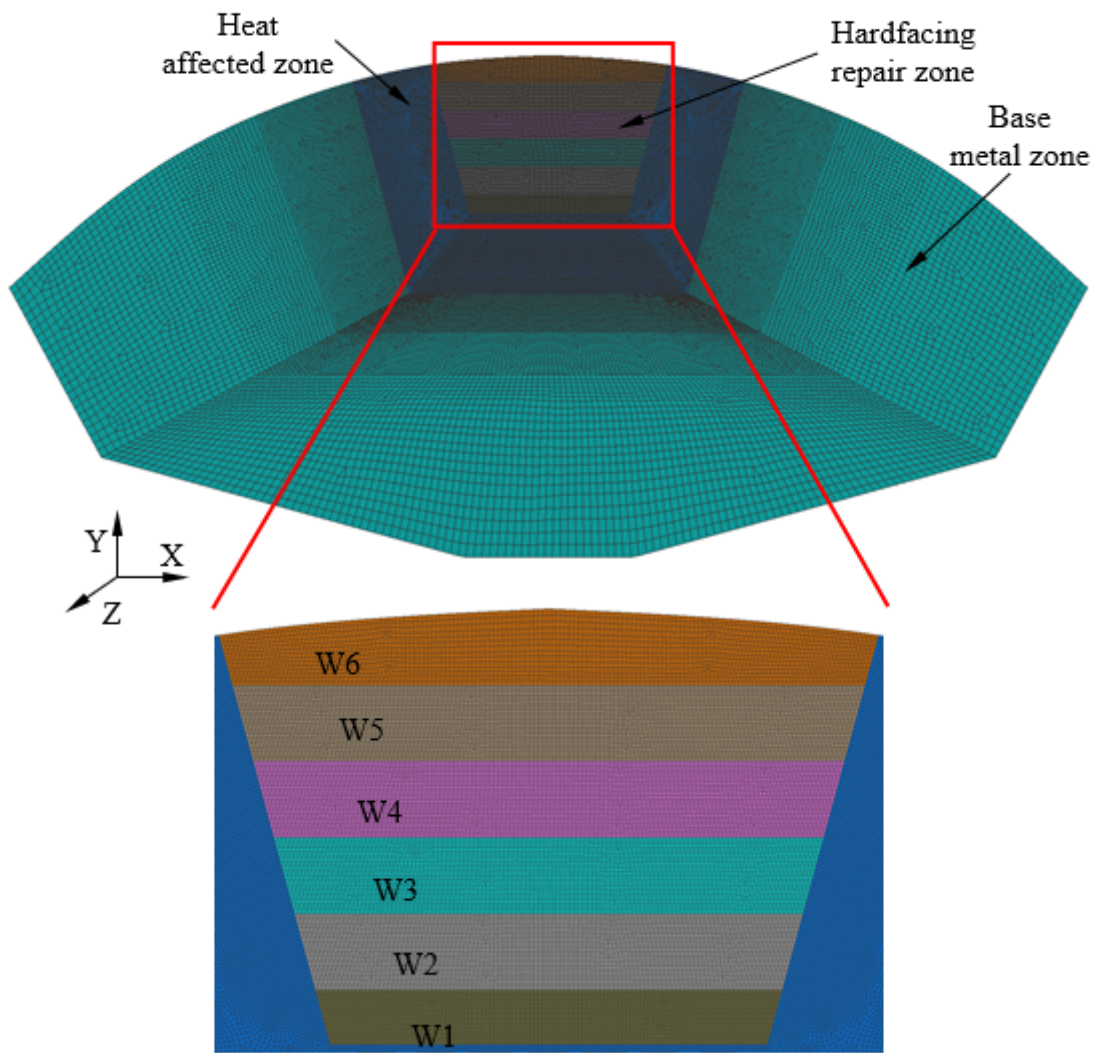


Figure 34

The global mesh model of grinding roller for remanufacturing

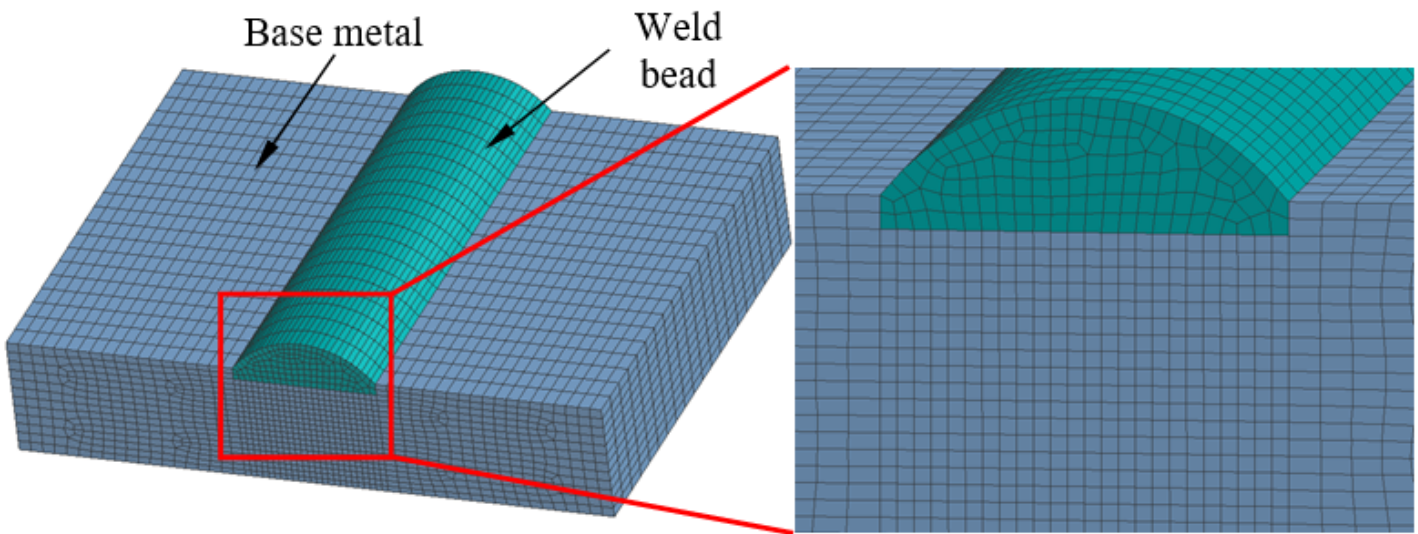


Figure 35

The local mesh model for heat source fitting

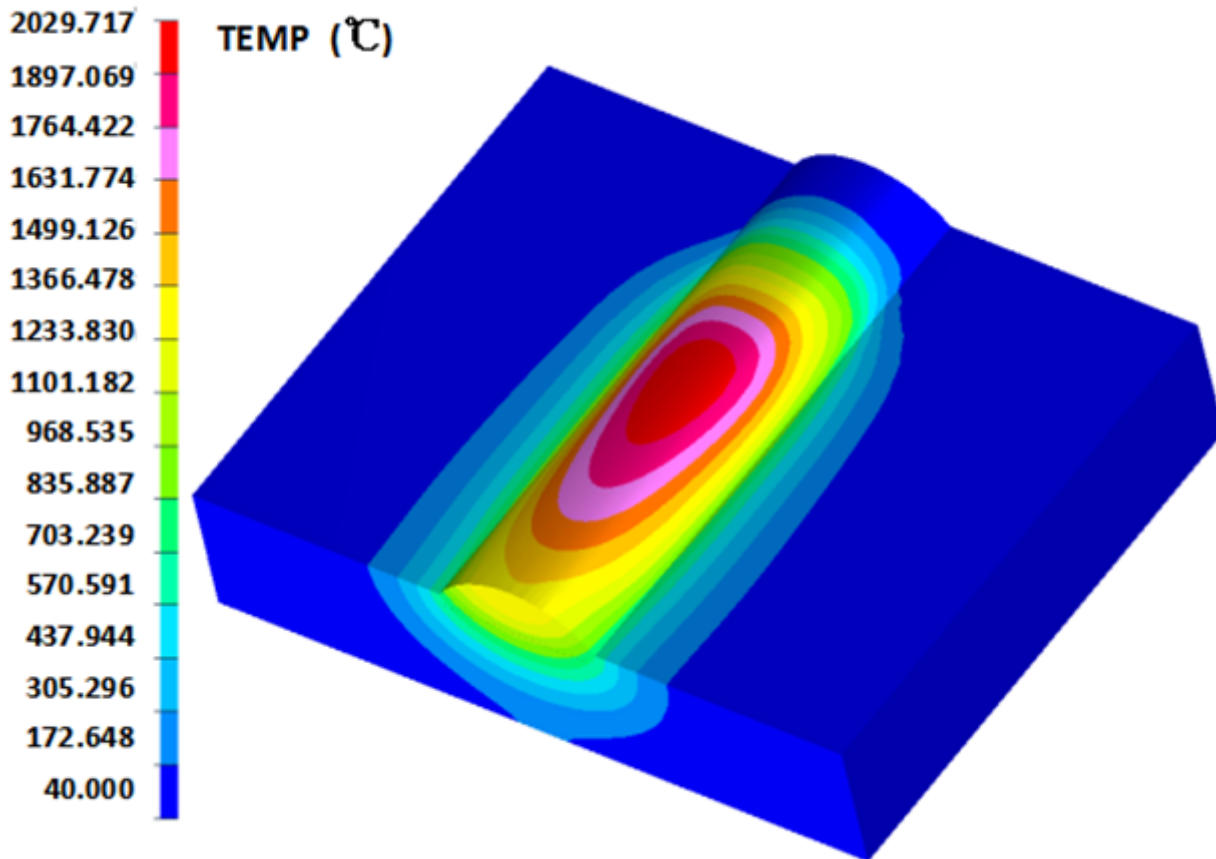


Figure 36

Steady-state temperature field of the bead-on-plate welding

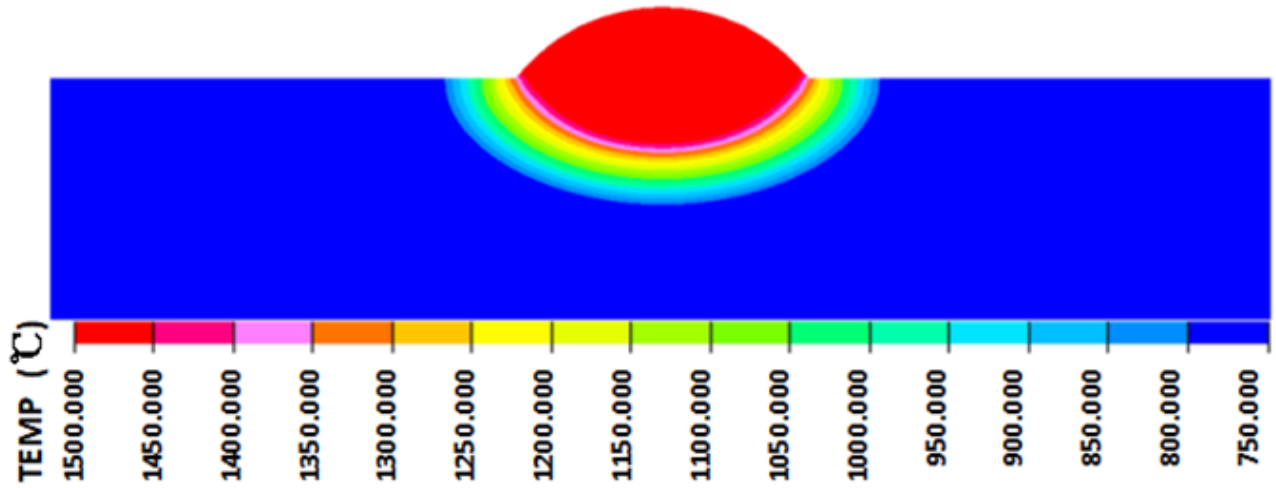


Figure 37

Simulated fusion zone (region of weld above 1500 °C) for heat source fitting

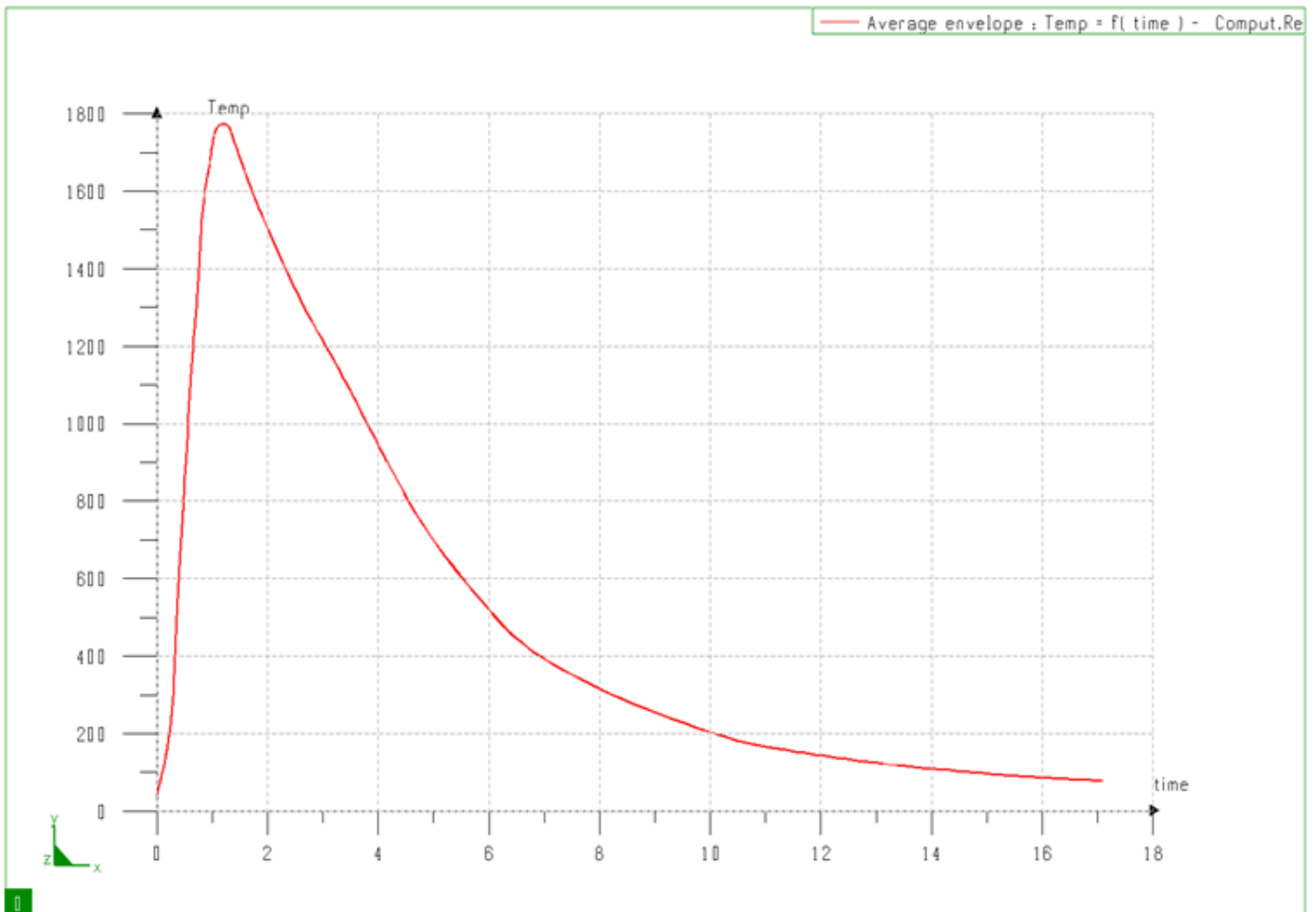


Figure 38

The average thermal cycle curve used for numerical simulation of hardfacing remanufacturing

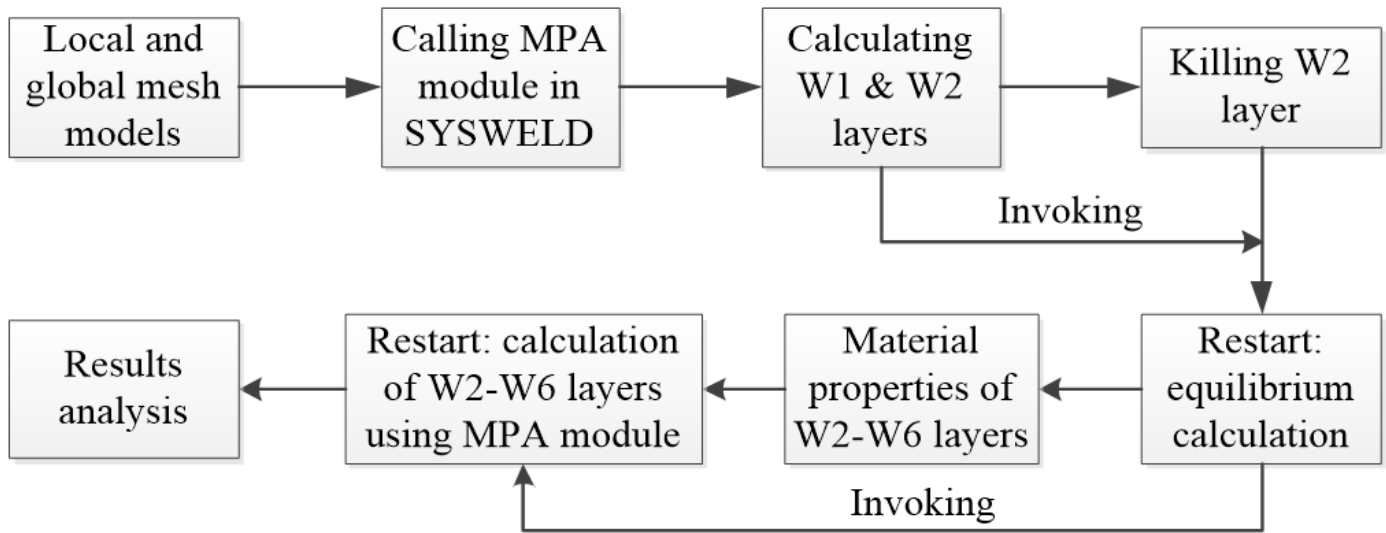


Figure 39

The calculation workflow of hardfacing remanufacturing for grinding roller

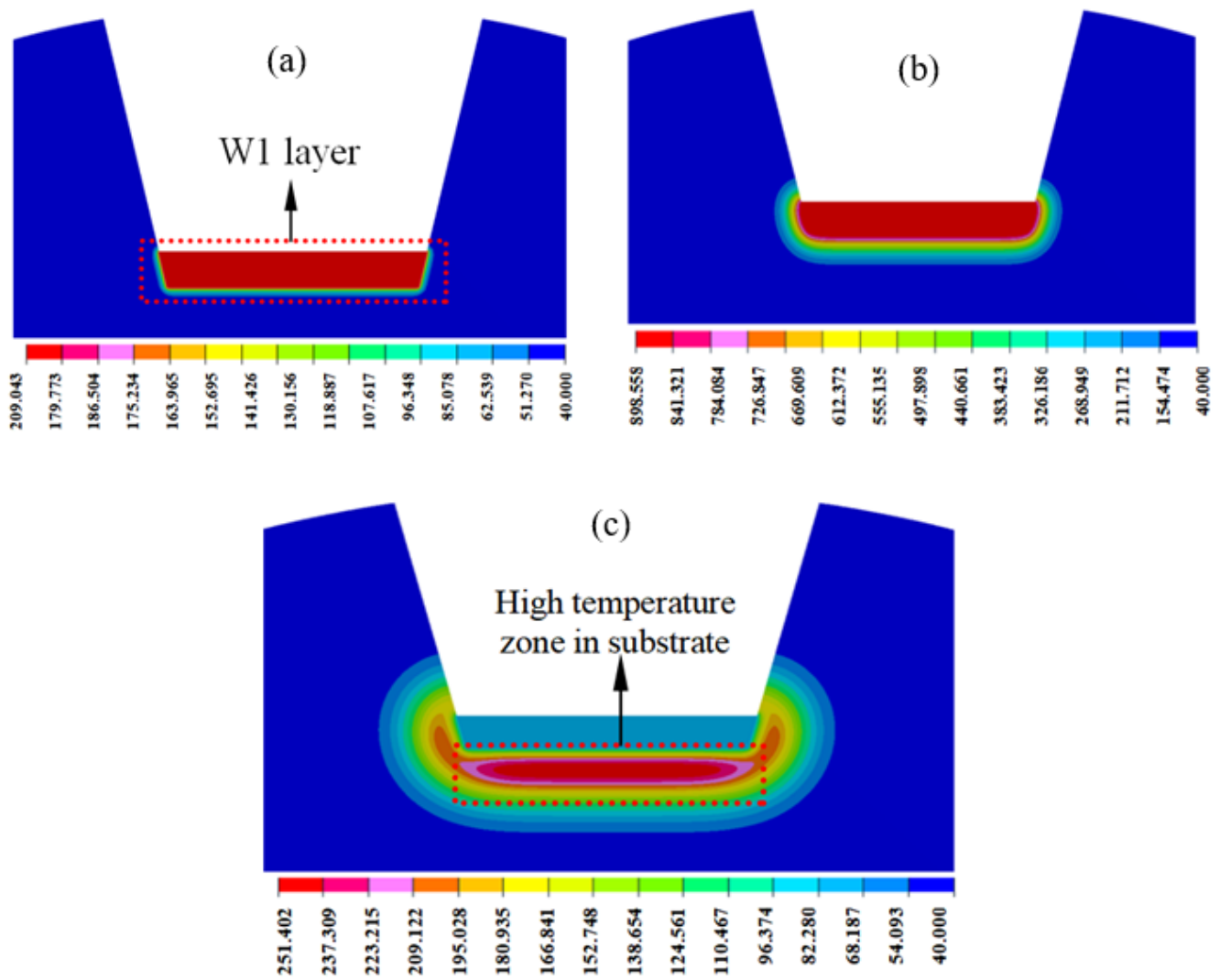


Figure 40

Temperature distribution of surfacing W1 at (a) $t=0.21s$; (b) $t=4.22s$; (c) $t=15s$.

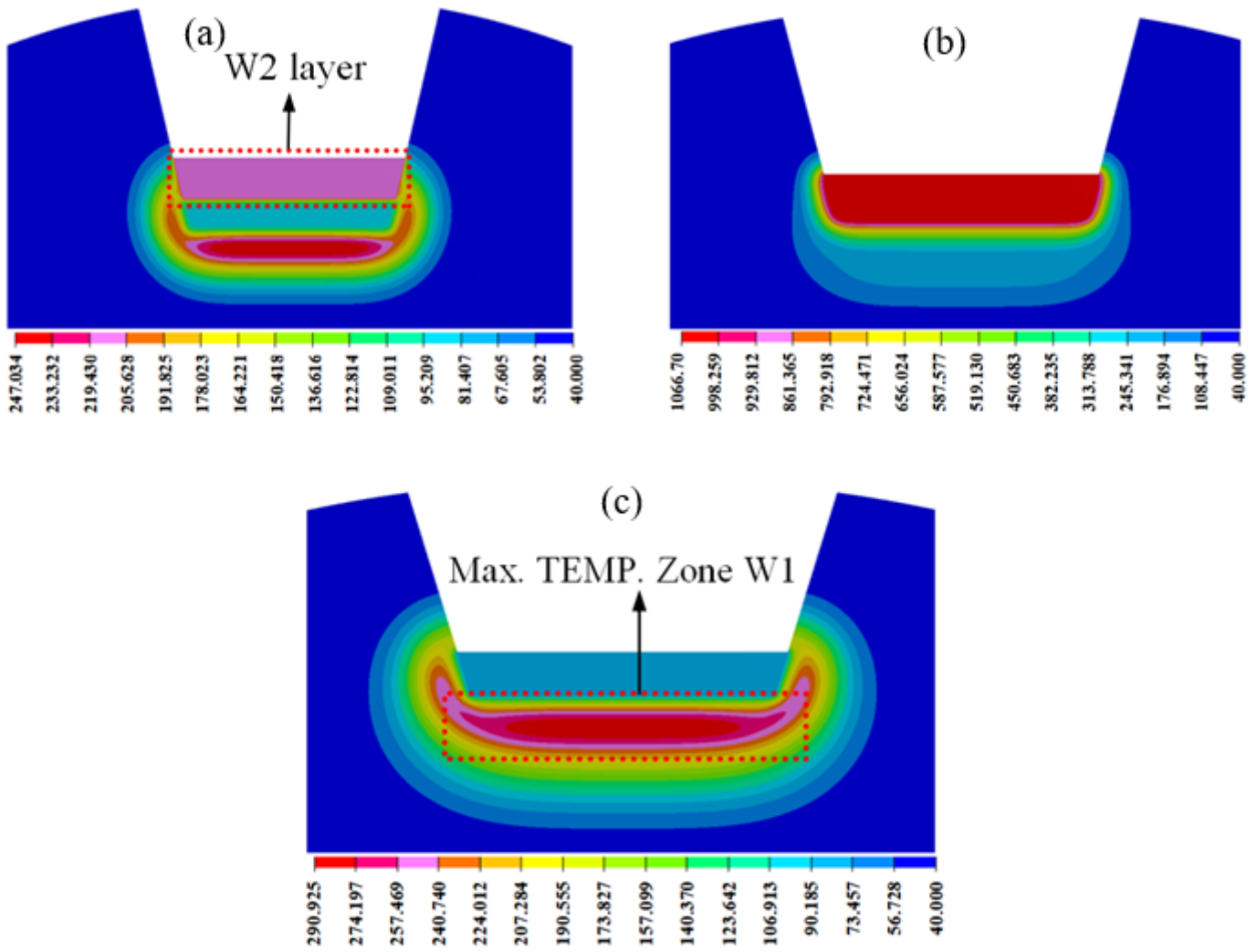


Figure 41

Temperature distribution of surfacing W2 at (a) $t=15.25s$; (b) $t=18.73s$; (c) $t=30s$.

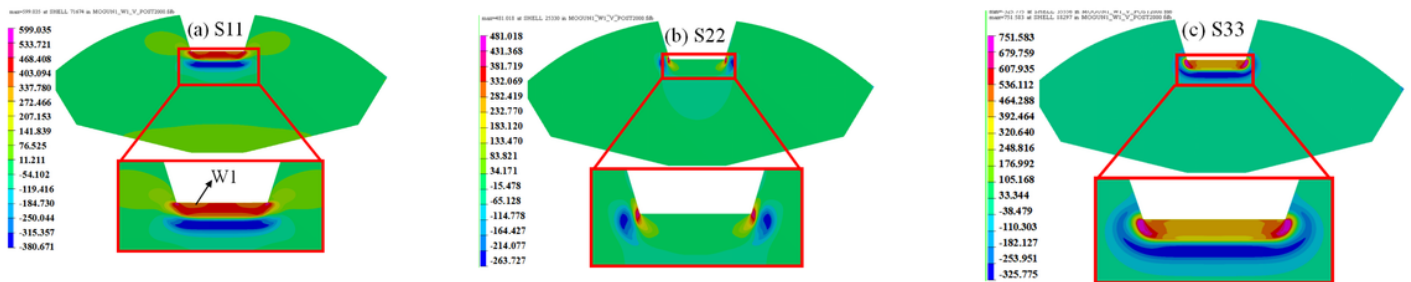


Figure 42

Residual stress induced by surfacing W1: (a) axial stress S11; (b) radial stress S22; (c) hoop stress S33.

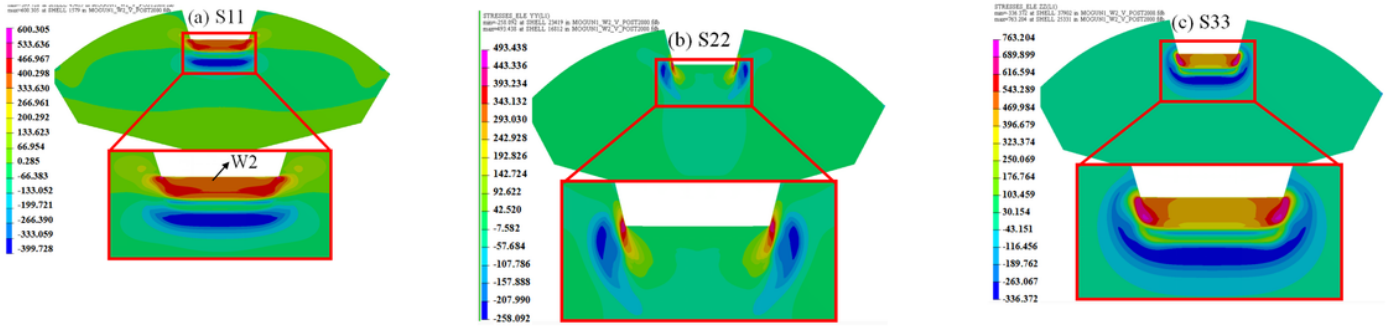


Figure 43

Residual stress induced by surfacing W2: (a) axial stress S11; (b) radial stress S22; (c) hoop stress S33.

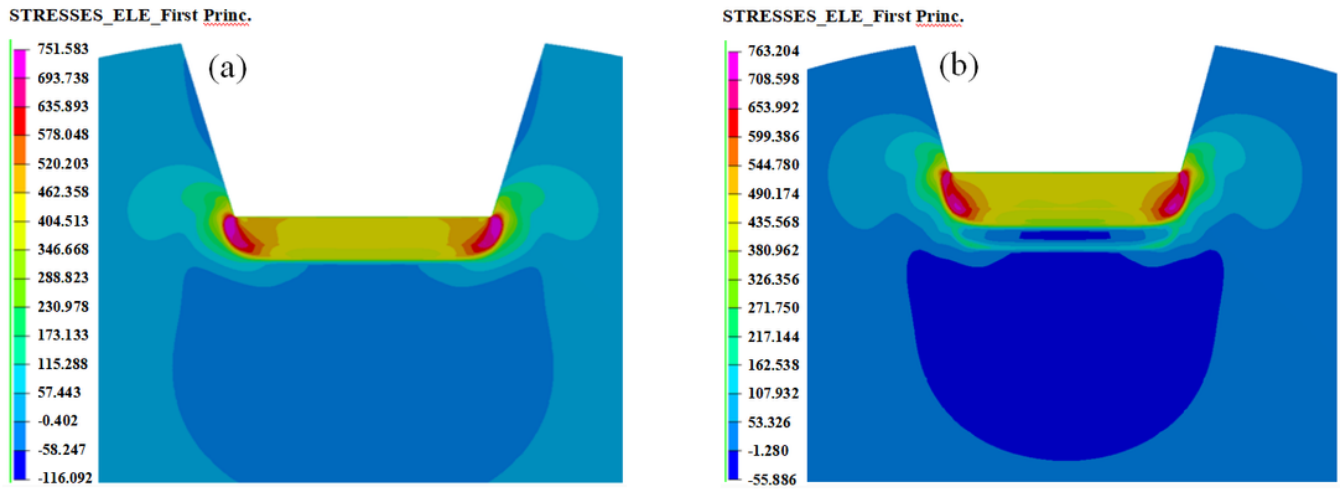


Figure 44

Maximal principal stresses distribution after each welding layer: (a) W1; (b) W2.

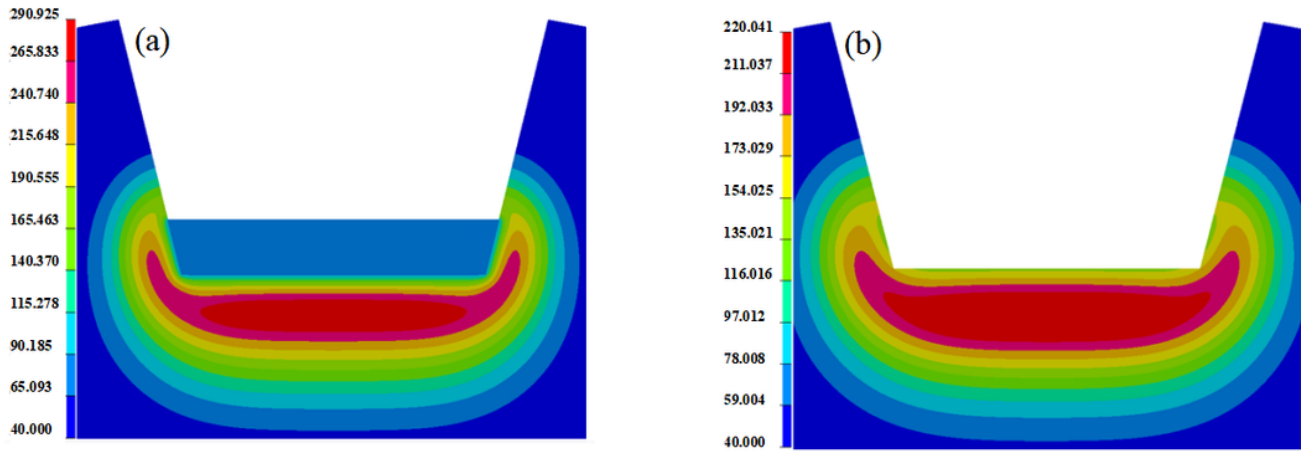


Figure 45

Temperature field before and after removing the weld pass: (a) before the removal of W2; (b) after the removal of W2.

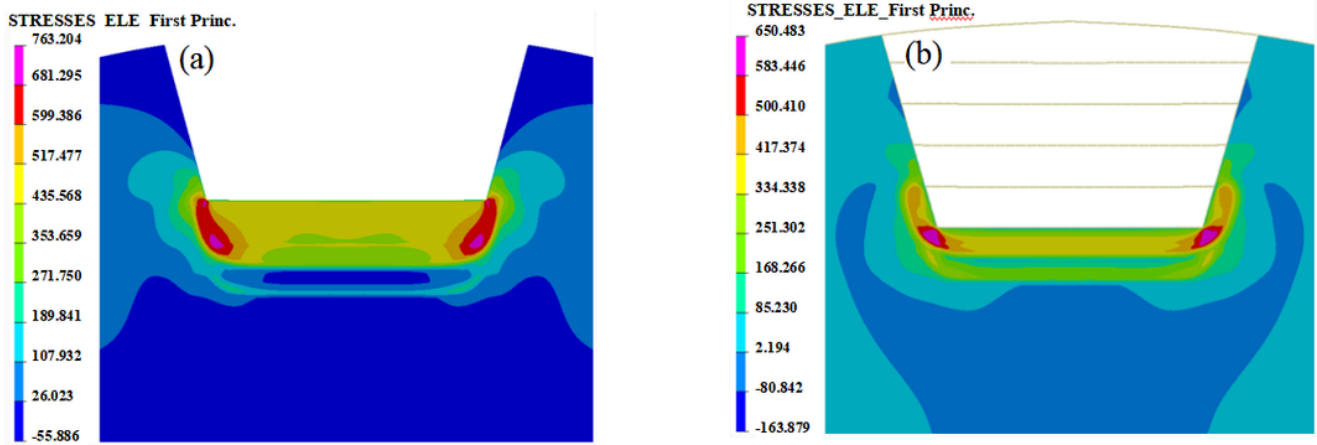


Figure 46

The maximal principal stresses before and after removing the weld pass: (a) before the removal of W2; (b) after the removal of W2.

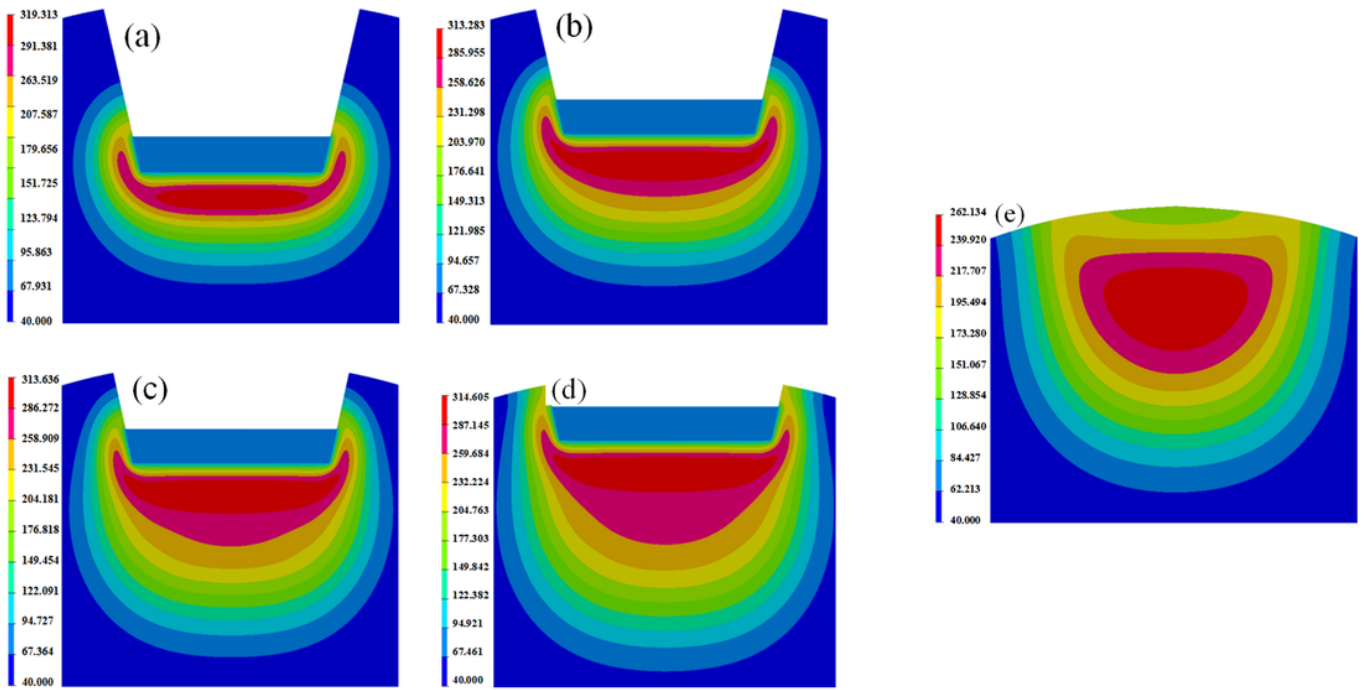


Figure 47

Temperature field after surfacing welding layers from W2 to W6: (a) W2; (b) W3; (c) W4; (d) W5; (e) W6.

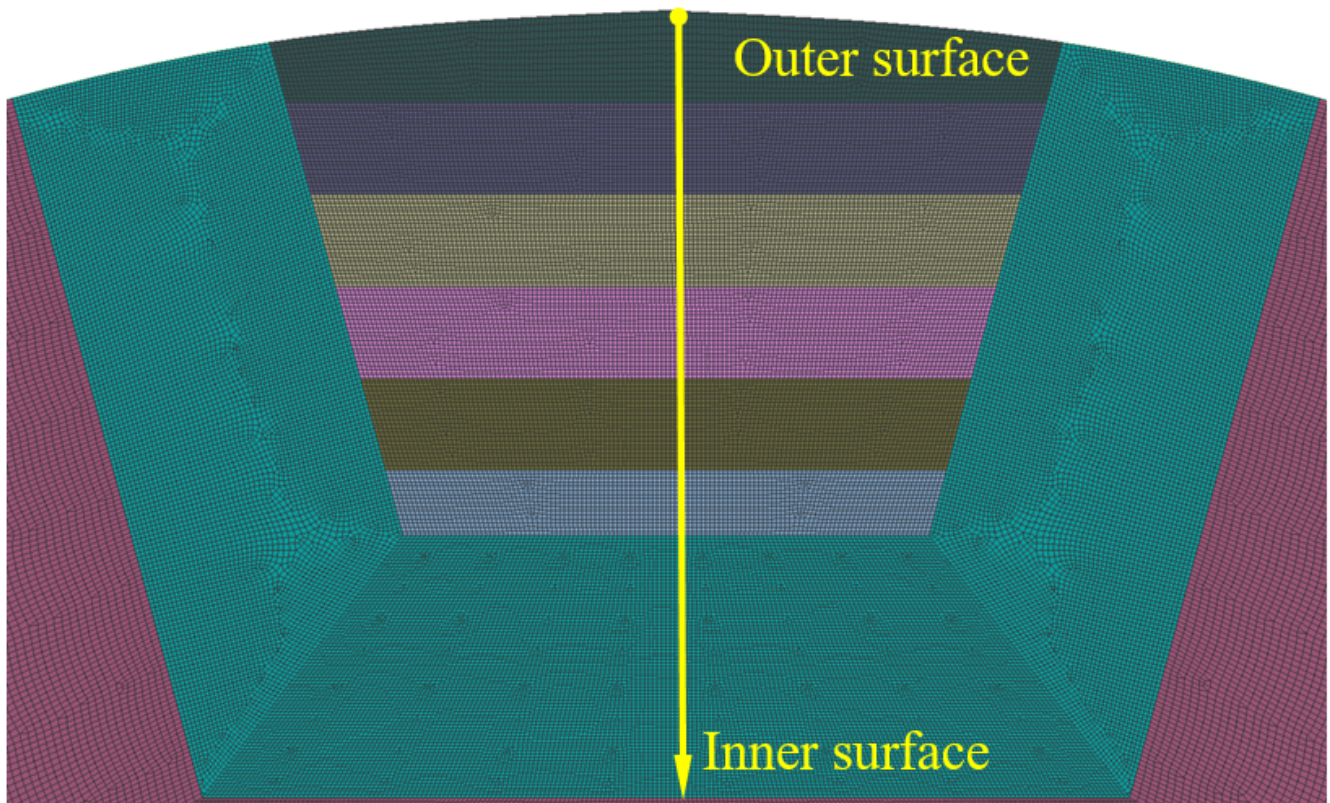


Figure 48

The measuring points along the line from outer surface to inner surface

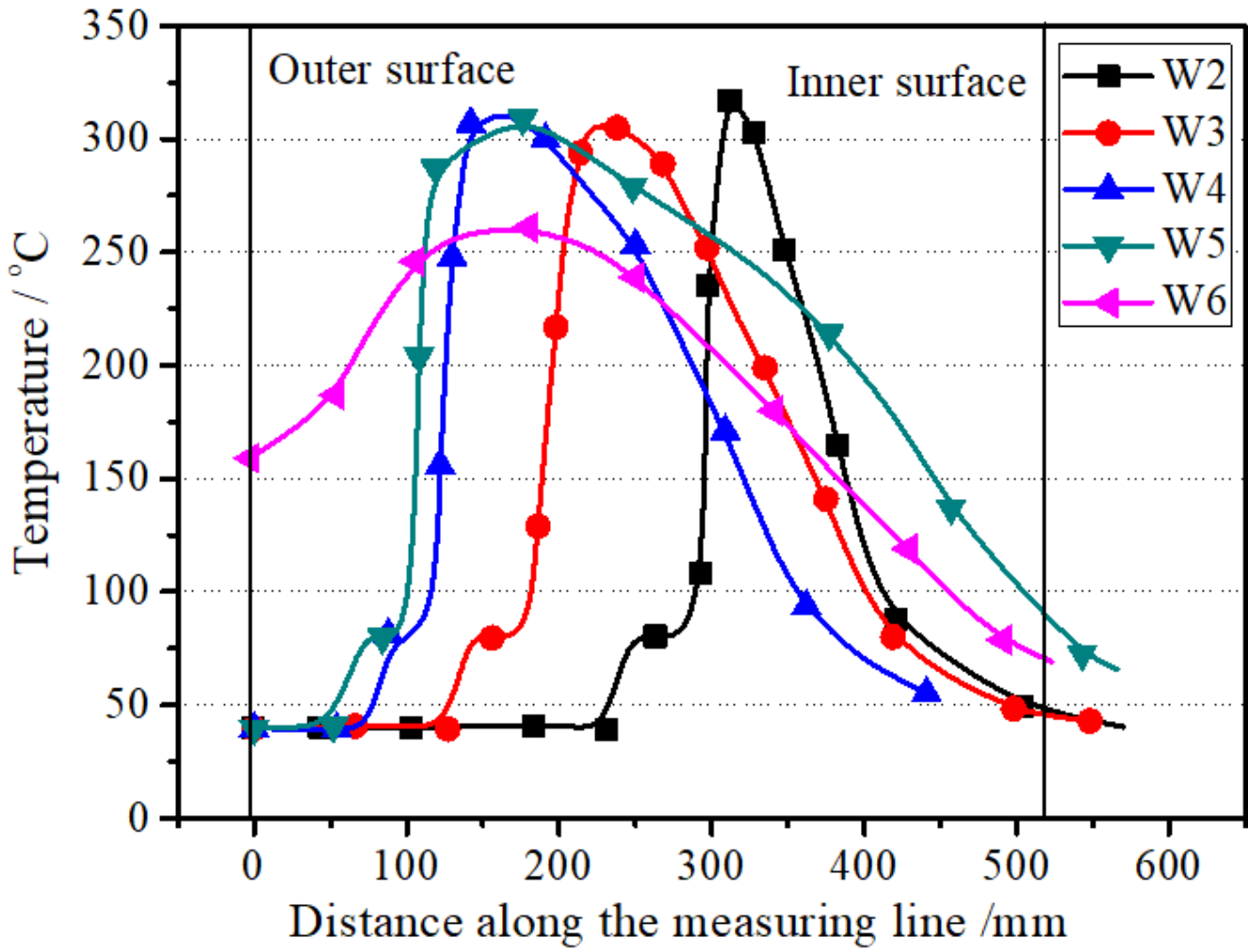


Figure 49

Temperature curves of different weld layers along the measuring line

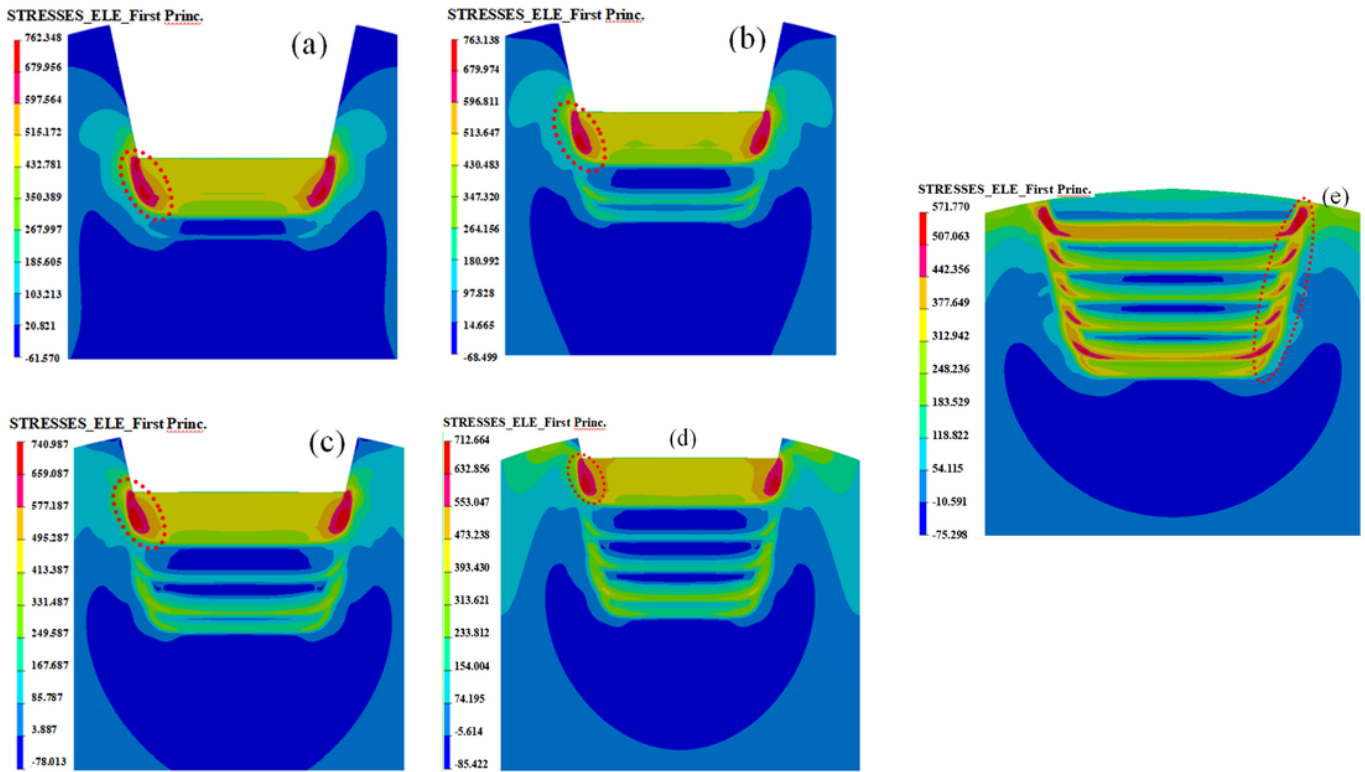


Figure 50

The maximal principal stresses distribution field after hardfacing from W2 to W6: (a) W2; (b) W3; (c) W4; (d) W5; (e) W6

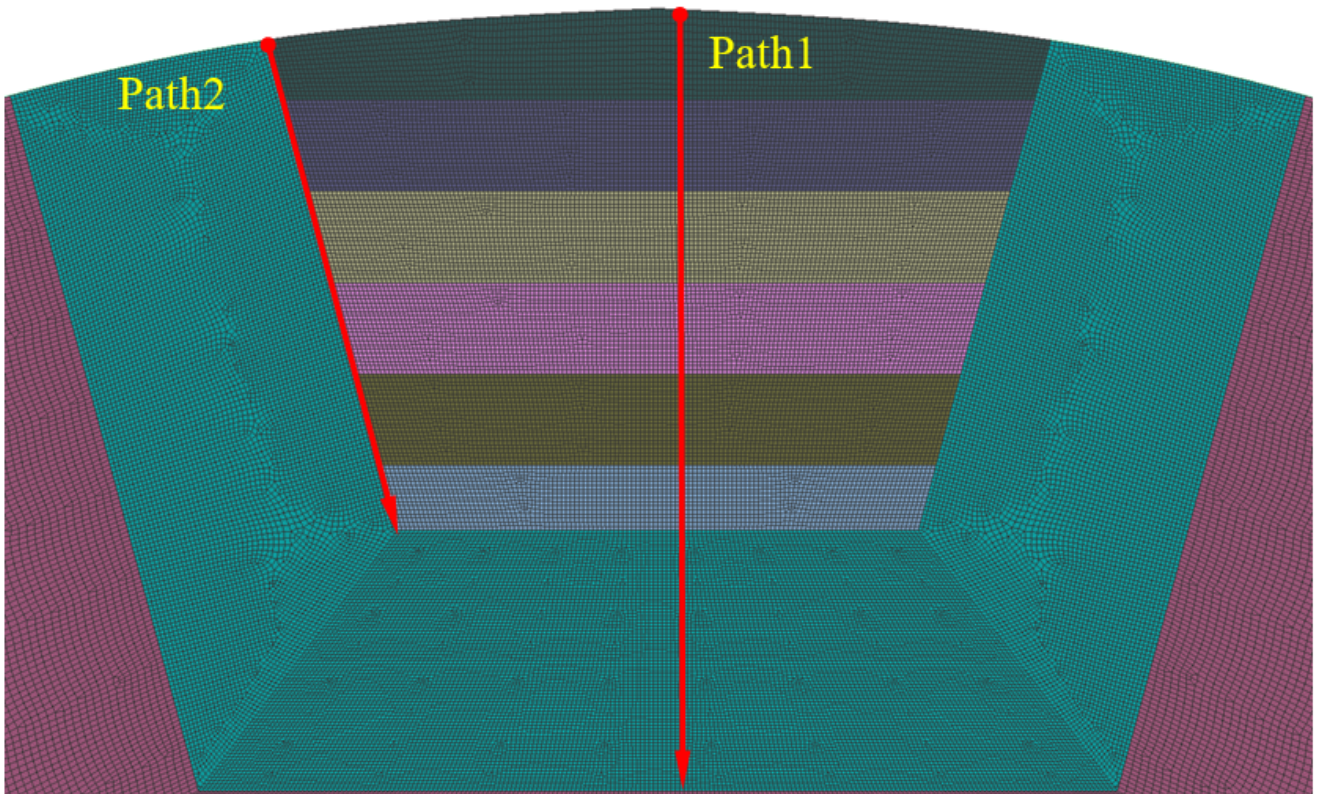


Figure 51

The measuring lines for residual stresses of grinding roller

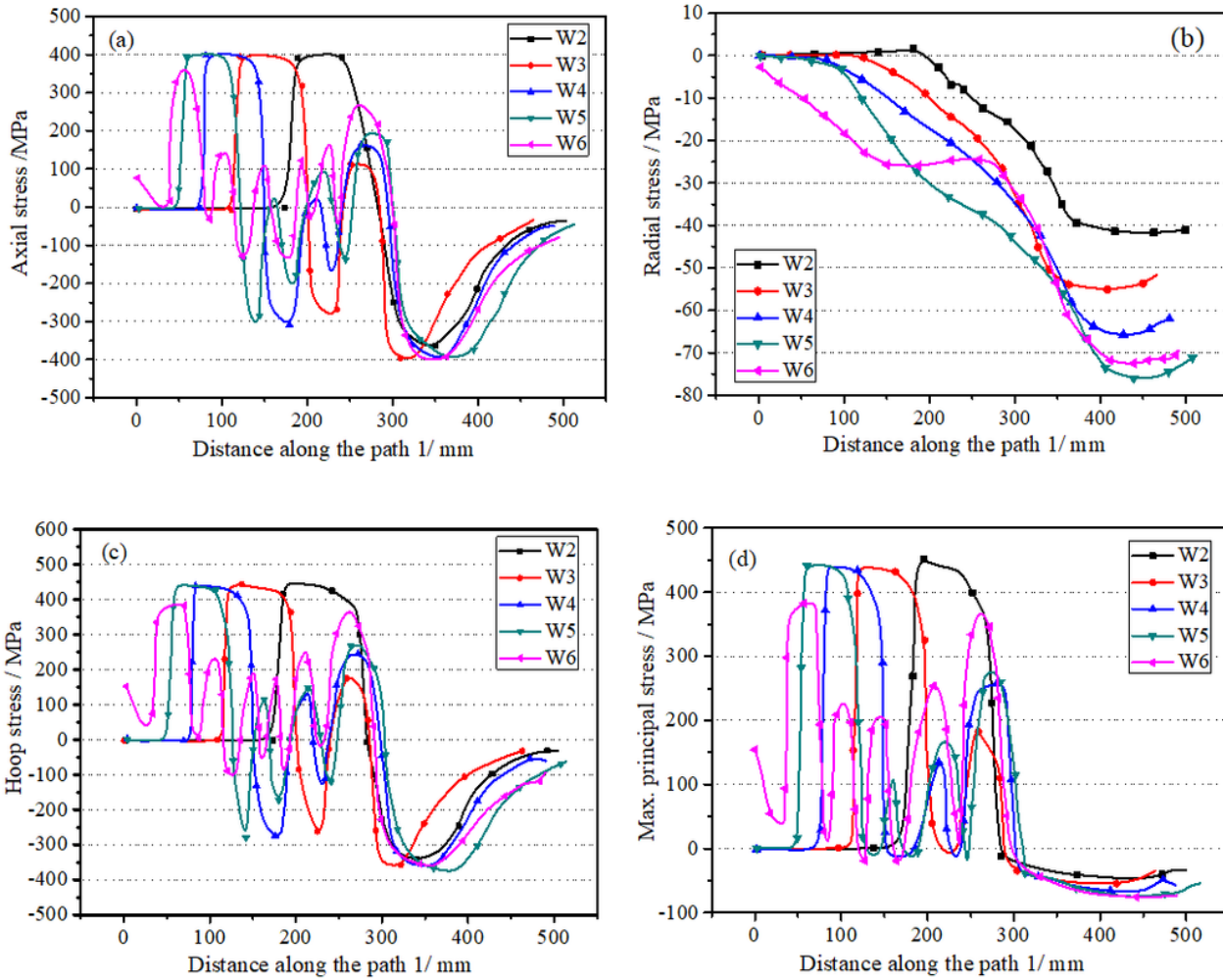


Figure 52

The residual stresses of different welding layers along path 1: (a) axial stress; (b) radial stress; (c) hoop stress; (d) maximal principal stress.

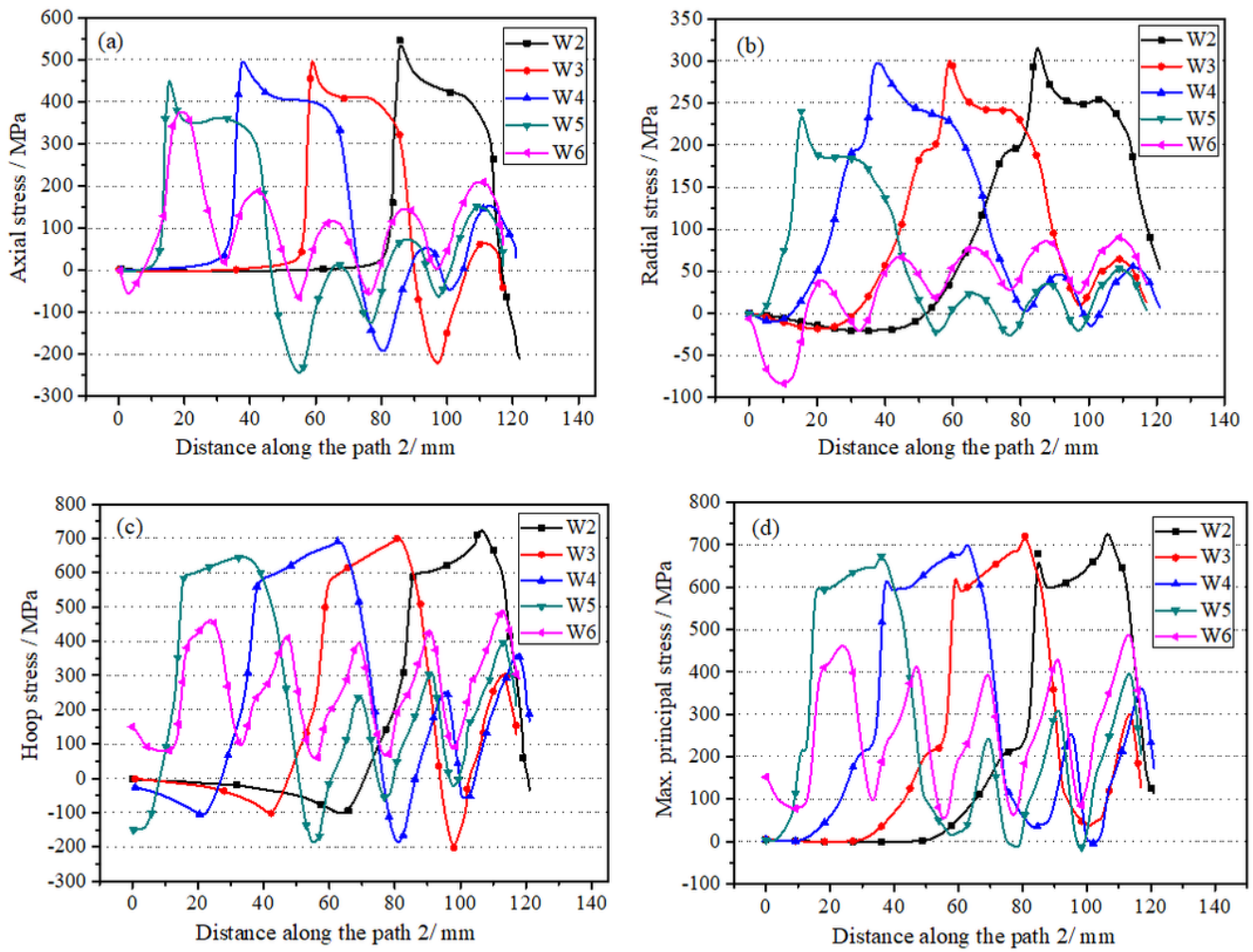


Figure 53

The residual stresses of different welding layers along path 2: (a) axial stress; (b) radial stress; (c) hoop stress; (d) maximal principal stress.

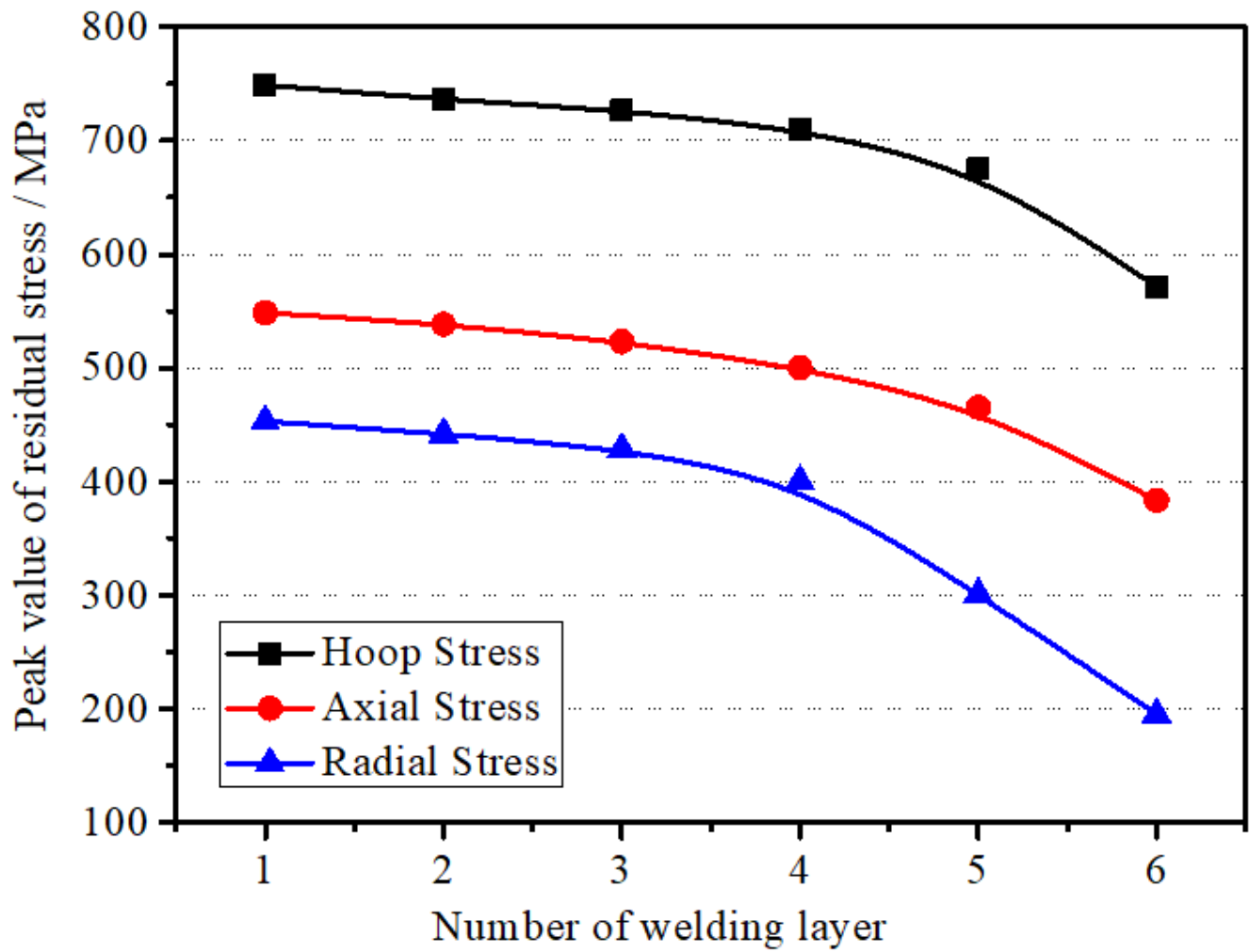


Figure 54

Effect of weld layers on peak stresses.

Supplementary Files

This is a list of supplementary files associated with this preprint. Click to download.

- [Tables.doc](#)